AGU PUBLICATIONS

JGR

Journal of Geophysical Research: Oceans

RESEARCH ARTICLE

10.1002/2016JC011682

Bottom pressure torque and the vorticity balance from observations in Drake Passage

Yvonne L. Firing[1,2], Teresa K. Chereskin[1], D. Randolph Watts[3], and Matthew R. Mazloff[1]

[1]Scripps Institution of Oceanography, University of California, San Diego, La Jolla, California, USA, [2]Now at National Oceanography Centre, Southampton, UK, [3]Graduate School of Oceanography, University of Rhode Island, Narragansett, Rhode Island, USA

Key Points:
- Local ACC vorticity budget dominated by nonlinear advection (mean and eddy) and ageostrophic divergence of horizontal velocity
- Drake Passage bottom pressure torque dominated by SAF/northern slope, averages 3×10^{-9} m s^{-2}, more than 10 times wind stress curl forcing
- Near-bottom flow in Drake Passage, and patterns of bottom pressure torque, not reflected directly in surface fields

Correspondence to:
Y. L. Firing,
yvonne.firing@noc.ac.uk

Citation:
Firing, Y. L., T. K. Chereskin, D. R. Watts, and M. R. Mazloff (2016), Bottom pressure torque and the vorticity balance from observations in Drake Passage, *J. Geophys. Res. Oceans*, *121*, 4282–4302, doi:10.1002/2016JC011682.

Received 26 JAN 2016
Accepted 19 MAY 2016
Accepted article online 26 MAY 2016
Published online 24 JUN 2016

Abstract The vorticity balance of the Antarctic Circumpolar Current in Drake Passage is examined using 4 years of observations from current- and pressure-recording inverted echo sounders. The time-varying vorticity, planetary and relative vorticity advection, and bottom pressure torque are calculated in a two-dimensional array in the eddy-rich Polar Frontal Zone (PFZ). Bottom pressure torque is also estimated at sites across Drake Passage. Mean and eddy nonlinear relative vorticity advection terms dominate over linear advection in the local (50-km scale) vorticity budget in the PFZ, and are balanced to first order by the divergence of horizontal velocity. Most of this divergence comes from the ageostrophic gradient flow, which also provides a second-order adjustment to the geostrophic relative vorticity advection. Bottom pressure torque is approximately one-third the size of the local depth-integrated divergence. Although the cDrake velocity fields exhibit significant turning with depth throughout Drake Passage even in the mean, surface vorticity advection provides a reasonable representation of the depth-integrated vorticity balance. Observed near-bottom currents are strongly topographically steered, and bottom pressure torques grow large where strong near-bottom flows cross steep topography at small angles. Upslope flow over the northern continental slope dominates the bottom pressure torque in cDrake, and the mean across this Drake Passage transect, 3 to 4×10^{-9} m s^{-2}, exceeds the mean wind stress curl by a factor of 15–20.

1. Introduction

The broad outlines of the momentum balance in the Antarctic Circumpolar Current (ACC) were described by *Munk and Palmén* [1951]: momentum input fairly uniformly over the course of the ACC by the wind stress is ultimately balanced principally by bottom form stress. In the corresponding vorticity balance, vorticity input by the wind stress curl is balanced by bottom pressure torque. These topographic balancing forces are likely to be enhanced in regions of greater bathymetric relief such as Drake Passage and the Scotia Sea, Kerguelen Plateau, and Campbell Plateau. Details of the contributions of particular regions to the mean vorticity balance, however, have not previously been well observed, nor have the details of the transfer of vorticity from the surface to the locations at the bottom where topographic forcing is applied.

Wells and de Cuevas [1995] found a first-order balance between circumpolar wind stress curl and bottom pressure torque in a model ACC, with bottom pressure torque generated primarily in the Drake Passage/Scotia Sea/Argentine Basin region and south of Tasmania and New Zealand. They also found that in the northern part of the ACC both advection and lateral friction added to wind stress curl, while in the south these two terms tended to compensate for each other. *Hughes and de Cuevas* [2001] confirmed that a numerical model zonally integrated barotropic vorticity balance is dominated by wind stress curl and bottom pressure torque, with locally large nonlinear terms. *Grezio et al.* [2005] found the same dominant balance, with an enhancement of both relative vorticity advection and bottom pressure torque near topography in several numerical models. *Thompson and Naveira Garabato* [2014] investigated the role of standing meanders and regions of elevated eddy kinetic energy in the vorticity balance in an eddy-resolving model. They found a local balance between stretching (the ageostrophic divergence of horizontal velocity) and relative vorticity advection, with advection dominating above 2000 m and divergence below, consistent with standing Rossby waves, and the magnitude of both terms correlated with the strength of quasi-standing meanders. The larger scales evident in the barotropic and time-mean vorticity balances in their model are consistent with slow propagation of these meanders.

Numerical models of the Southern Ocean [*Killworth*, 1992; *Hughes and Killworth*, 1995; *Killworth and Hughes*, 2002] exhibit an equivalent-barotropic vertical structure in the ACC: that is, pressure and density contours are parallel, so that the current does not turn significantly with depth. This structure arises because the variation of the Coriolis parameter with latitude and the vertical gradient of vertical velocity are both second order [*Killworth*, 1992; *Killworth and Hughes*, 2002]; in models this condition tends to be violated only in limited locations near topography [*Hughes and Killworth*, 1995; *Killworth and Hughes*, 2002]. Mean velocities in the data-assimilating Southern Ocean State Estimate (SOSE) [*Mazloff et al*., 2010] rotate with depth mostly outside or below the jet centers, and where flow goes over topography [*Peña-Molino et al*., 2014]. Moored [*Ferrari et al*., 2012] and drifting [*Phillips and Bindoff*, 2014] velocity observations, including measurements in proximity to topography, reveal time-varying velocities which turn significantly with depth, but much smaller turning in the mean.

Hughes [2005] used the mean surface dynamic topography of *Niiler et al*. [2003] and an assumption of equivalent-barotropic vertical structure to examine the mean nonlinear vorticity balance of the ACC. He described two regimes: a wave-like one in regions of smooth bathymetry in which the surface planetary and mean relative vorticity advection balanced (with a wavelength consistent with stationary Rossby waves with small net depth-integrated divergence); and in regions of enhanced bathymetry (including Drake Passage) a regime in which planetary vorticity advection dominated over relative vorticity advection. *Chereskin et al*. [2010] confirmed the first type of balance, between planetary and relative vorticity advection, from direct velocity observations in the Subantarctic Front in the southeast Pacific. *Hughes* [2005] suggested that the planetary vorticity advection in the second regime would be balanced by bottom pressure torque, which would likely be elevated in those regions. The direct measurements of bottom currents described here will demonstrate a different local balance in Drake Passage.

Hughes and Ash [2001] and *Williams et al*. [2007] examined eddy forcing of the mean ACC using satellite altimeter sea level anomaly data, and found significant surface eddy vorticity fluxes in areas where the current appears to be topographically steered, including Drake Passage. In the OFES (Ocean General Circulation for the Earth Simulator) model, relative vorticity provides a coupling between shallow and deep currents in high-eddy kinetic energy regions downstream of standing meanders [*Thompson and Naveira Garabato*, 2014]. Changes in the relative sizes of jets and eddies with depth, along with observations of large near-bottom eddy velocities ($O(10)$ cm s^{-1}) [*Chereskin et al*., 2009], imply that deep eddy fluxes may also be nonnegligible.

An observational examination of the subsurface contributions to the ACC vorticity balance could help confirm or refute the dynamics and balance inferred from surface data [e.g., *Hughes*, 2005; *Williams et al*., 2007] and numerical models [e.g., *Wells and de Cuevas*, 1995; *Hughes and de Cuevas*, 2001; *Grezio et al*., 2005; *Thompson and Naveira Garabato*, 2014]. In this paper, we investigate the vorticity balance of the ACC in Drake Passage using a 4-year time series of measurements by current and pressure recording inverted echo sounders (CPIES) deployed across Drake Passage as part of the cDrake project [*Chereskin et al*., 2012], as well as a 9-year time series of shipboard acoustic Doppler current profiler (SADCP) velocities in Drake Passage, SOSE, and 21 years of satellite altimeter fields. Data sources and methods for computing vorticity balance terms are described in section 2. We examine observed near-bottom velocities, mapped bottom geostrophic stream function, and the corresponding bottom pressure torques in section 3. In section 4, we discuss the vertical structure of the time-varying and time-mean cDrake velocity fields. We examine the mapped relative vorticity and mean and eddy relative vorticity advection fields in the cDrake LDA in section 5 and the LDA vorticity balance in section 6. We discuss our results in section 7 and summarize in section 8.

2. Data and Methods

2.1. cDrake

As part of the cDrake experiment [*Chereskin et al*., 2012], 42 CPIES were deployed across Drake Passage from November–December 2007 to November–December 2011 (Figure 1). The CPIES measure velocity 50 m above the bottom (outside the bottom boundary layer), bottom pressure, and bottom-to-surface round-trip acoustic travel time. The 3 × 7 Local Dynamics Array (LDA, Figure 1), with 37-km instrument spacing, was positioned in the eddy-rich Polar Frontal Zone (PFZ) just downstream of the Shackleton Fracture Zone (SFZ) and designed to cover a meander wavelength (200–250 km) [*Chereskin et al*., 2010; *Rocha*

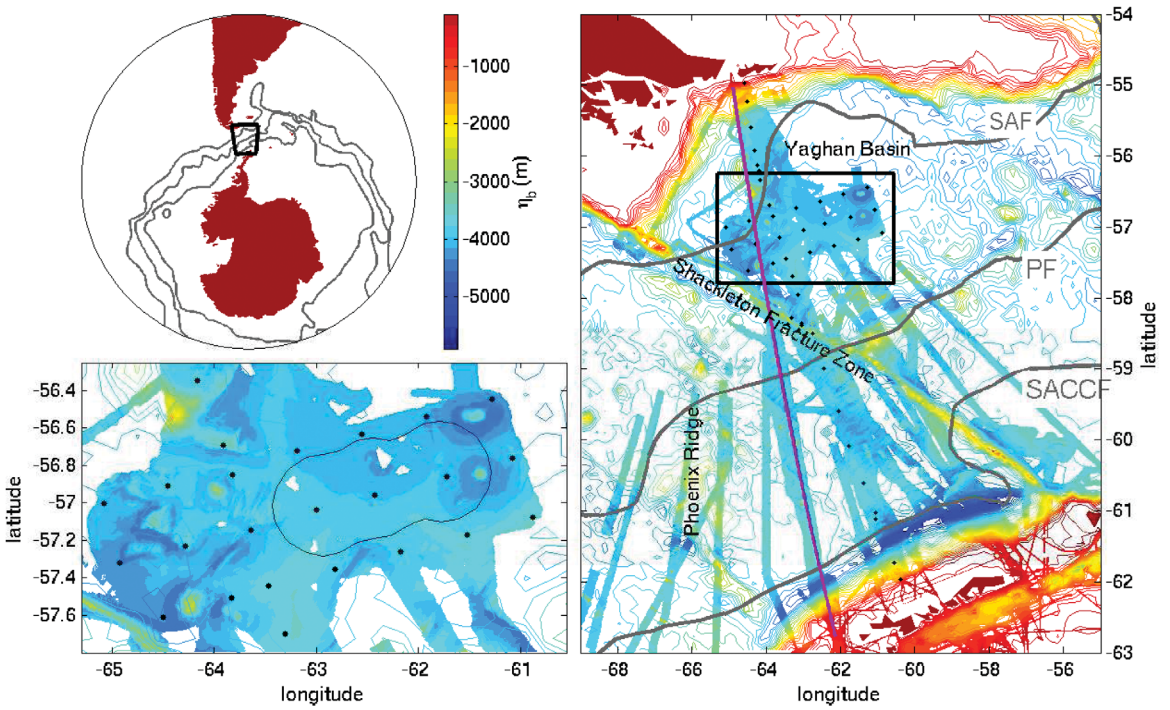

Figure 1. Drake Passage area with cDrake CPIES sites (black dots) over bathymetry η_b from *Smith and Sandwell* [1997] (color contour lines) and RVIB NB Palmer multibeam database (filled color contours). Gray curves show climatological front positions from *Orsi et al.* [1995]. Purple line shows the most common LM Gould track. The LDA area is enlarged at bottom left, and the subarea in the central-eastern LDA from which time series are shown is outlined.

et al., 2016]. The cDrake CPIES data and processing are described in *Tracey et al.* [2013] and *Firing et al.* [2014]. Multibeam bathymetry data were also collected and processed on each of the five cDrake cruises, providing high-resolution bathymetry around the CPIES sites (Figure 1); these data are averaged to 2-km resolution, and gaps are filled by linear interpolation from the *Smith and Sandwell* [1997] bathymetric database.

2.1.1. Objectively Mapped Geostrophic Fields

The application of objective mapping to the cDrake observations is described by Firing et al. [2014] and summarized here. Bottom pressures and near-bottom currents are objectively mapped to a 4000 dbar reference (hereafter referred to as barotropic) geostrophic stream function ψ, horizontal velocity $\mathbf{u}_g=(u_g,v_g)=(-\partial\psi/\partial y,\partial\psi/\partial x)/f$, vertical relative vorticity $\zeta_g=\partial v_g/\partial x-\partial u_g/\partial y$, and relative vorticity gradients $\partial\zeta_g/\partial x$ and $\partial\zeta_g/\partial y$, using the geostrophic continuity constraint $\nabla_H\cdot(f\mathbf{u}_g)=\nabla_H\times\nabla_H\psi=0$ (where ∇_H is the horizontal gradient operator). Bottom-to-surface round-trip acoustic travel times are converted to profiles of geopotential anomaly by use of a Gravest Empirical Mode (GEM) [*Meinen and Watts*, 2000; *Watts et al.*, 2001] lookup table, and geopotential anomaly at each depth is then objectively mapped to baroclinic geostrophic stream function, velocity, relative vorticity, and relative vorticity gradients. While the baroclinic fields are (by construction) self-similar with depth, the degree of turning with depth of the total current depends on the relative directions and magnitudes of the barotropic and baroclinic components (Figure 2).

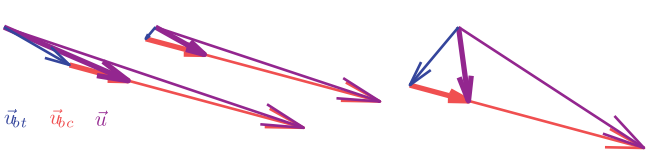

Figure 2. Idealized illustration of combinations of barotropic current $\mathbf{u}_{bt}$ (blue) with self-similar deep (thick vectors) and shallow (thin vectors) baroclinic currents $\mathbf{u}_{bc}$ (red), such as those produced by a GEM. In the left example, the total current u (purple) is approximately equivalent-barotropic, turning by $\ll 1$ rad over the depth range (note that this criterion could also be met by a very weak baroclinic current such that the total current was close to the barotropic current at all depths); in the middle, the current is approximately equivalent-barotropic except at the bottom, and in the right example the two components have both different orientations and similar magnitudes, such that the net turning with depth > 1 rad.

The objective mapping procedure iterates through three sets of time and space scales: the time mean, mapped at 200 km; the 61-day low-pass filtered

anomaly, mapped at 60 km, and the residual (effectively a 61-day high-pass filtered series), mapped at 50 km (spatial scales are determined based on decorrelation distances of filtered observed time series) [*Firing et al.*, 2014]. *Firing et al.* [2014] also describe validation of the accuracy of the cDrake maps by numerical simulations and comparison with independent measurements, indicating that vorticity balance terms can be resolved above the level of their uncertainty at periods of 7 days and longer. To examine 4-year time series and the dominant terms at various time scales, we use additional smoothing, applying Butterworth filters with cutoff periods of 30 days (plotted) or longer (not shown). We will refer to the variables computed from the CPIES data by objective mapping and the GEM as cDrake mapped or geostrophic velocity, vorticity, and so on.

2.1.2. Ageostrophic Contributions

Although ageostrophic residual velocities (from the directly measured near-bottom total velocities) are small compared to the mapped geostrophic velocities, the ageostrophic contribution to divergence and relative vorticity gradients depends not only on the size of ageostrophic currents but also on their spatial variability. Previous work [*Thompson and Naveira Garabato*, 2014] suggests that relative vorticity advection in the interior is primarily balanced by ageostrophic divergence of the horizontal flow, and episodic high values of Rossby number in the LDA (see section 5) point to a possibly significant cyclostrophic contribution. We estimate the combined gradient flow [*Holton*, 1979] as follows:

$$\kappa|\mathbf{u}|^2+f|\mathbf{u}|=\frac{1}{\rho}\frac{\partial p}{\partial n}=f|\mathbf{u}_g|, \tag{1}$$

where n is the direction normal to the total flow, $|\mathbf{u}|$ and $|\mathbf{u}_g|$ are the total and geostrophic horizontal speeds, respectively, and

$$\kappa \simeq \kappa_g=\frac{-\psi_{xx}\psi_y^2-\psi_{yy}\psi_x^2+2\psi_{xy}\psi_x\psi_y}{(\psi_x^2+\psi_y^2)^{3/2}} \tag{2}$$

is the curvature of the flow, here approximated using the objectively mapped derivatives of geostrophic stream function ψ [*Watts et al.*, 1995]. There is a slight preference for negative κ_g in the cDrake LDA, reflecting the slight preference for cyclonic circulations (see section 5) and associated subgeostrophic flow. We then have the total gradient wind velocity,

$$\mathbf{u}=\frac{2\mathbf{u}_g}{1+\sqrt{1+4\kappa_g|\mathbf{u}_g|/f}}, \tag{3}$$

where we have chosen the solution of (1) that gives $\mathbf{u}(\kappa_g \to 0)=\mathbf{u}_g$. We then estimate the relative vorticity ζ, relative vorticity gradients $\partial\zeta/\partial x$ and $\partial\zeta/\partial y$, and the vertical derivative of vertical velocity,

$$\partial w/\partial z=-\nabla_H\cdot\mathbf{u}, \tag{4}$$

by finite differencing of the total (horizontal) gradient wind flow $\mathbf{u}$. We will refer to the difference between the total gradient wind-derived fields and the objectively mapped geostrophic fields as the ageostrophic cDrake velocity,

$$\mathbf{u}_a=\mathbf{u}-\mathbf{u}_g, \tag{5}$$

and similarly ageostrophic vorticity, divergence, and so on. We estimate uncertainties on these fields by propagation of error through the finite differences; because this method does not incorporate spatial correlations, the resulting uncertainties are overestimates [see *Firing et al.*, 2014].

2.1.3. Vorticity Budget Terms

We use the cDrake mapped (geostrophic) and ageostrophic velocity, vorticity, and vorticity gradient fields to estimate terms of the quasi-geostrophic vertical vorticity balance,

$$\zeta_t+\mathbf{u}\cdot\nabla_H\zeta+\beta v-fw_z=\frac{1}{\rho_0}\nabla_H\times\tau_z, \tag{6}$$

where subscripts indicate derivatives, $\beta=df/dy$ is the meridional gradient of the Coriolis parameter f, w is the vertical velocity, $\rho_0=1050$ kg m^{-3} is a constant reference density, and τ is stress. The vortex stretching term, fw_z, is calculated from the divergence of horizontal velocity: $w_z=-(u_x+v_y)=-(u_{a,x}+v_{a,y})-\beta v_g/f$. The

vorticity tendency ζ_t, relative vorticity advection $\mathbf{u}\cdot\nabla_H\zeta$, planetary vorticity advection βv, and vortex stretching $-fw_z$ are balanced by the vertical divergence of stress curl $(1/\rho_0)\nabla_H\times\tau_z$. Neglected terms in (6) include nonlinear stretching (ζw_z), tilting ($\mathbf{u}_z\times\nabla_H w$), and lateral stress divergences.

The depth-integrated vorticity balance is then

$$\int_{\eta_b}^{0}\zeta_t dz+\int_{\eta_b}^{0}\mathbf{u}\cdot\nabla_H\zeta dz+\beta V+fw_b=\frac{1}{\rho_0}\nabla_H\times\tau_w-\frac{1}{\rho_0}\nabla_H\times\tau_b, \tag{7}$$

where $z=\eta_b<0$ is the bottom coordinate, $V=\int_{\eta_b}^{0}v dz$, w_b is bottom vertical velocity, τ_w is surface wind stress, and τ_b bottom frictional stress. For a predominantly geostrophic flow, the vortex stretching due to flow over topography, $fw_b=f\mathbf{u}_b\cdot\nabla_H\eta_b$, will be dominated by $J(p_b,\eta_b)=f\mathbf{u}_{b,g}\cdot\nabla_H\eta_b$, the negative of the bottom pressure torque, where p_b is the bottom pressure and $\mathbf{u}_{b,g}$ the bottom geostrophic velocity. As discussed above, the bottom pressure torque is also expected to outweigh the bottom frictional torque. Thus, in the full-depth quasi-geostrophic balance, the depth integrals of vorticity tendency, nonlinear relative vorticity advection, and linear planetary vorticity advection are balanced by bottom pressure torque and the vorticity forcing due to wind stress curl.

As $\mathbf{u}_a\ll\mathbf{u}$ and $\zeta_a\ll\zeta_g$, we compute planetary vorticity advection directly from cDrake mapped (geostrophic) velocity, and vorticity tendency by finite time-differencing of the cDrake mapped vorticity fields. We use both the mapped and total velocity and relative vorticity gradient fields to compute relative vorticity advection and horizontal divergence.

We use the mapped geostrophic bottom reference currents and high-resolution bottom topography to compute bottom pressure torque, $-J(p_b,\eta_b)/\rho_0=-f\mathbf{u}_{b,g}\cdot\nabla_H\eta_b$. Bathymetry gradients are estimated by first-differencing the 2-km data (see above) and further smoothed by Gaussian-weighted averaging to the objective mapping grid. We are interested in bathymetry gradients at the scales that influence the mesoscale flow sampled by the cDrake array outside the bottom boundary layer. *Bishop et al*. [2012] suggest that relatively small seamounts can affect the geostrophic flow at larger scales, so we tested length scales ranging from 10 to 50 km (the shortest objective mapping scale) for the bathymetry gradient weighted averaging. We will show the 50-km-smoothed bathymetry and resulting bottom pressure torques in both sections 3 and 6, but consider the values produced by less-smooth fields as a measure of uncertainty. We also compute total vortex stretching either as $-fw_b=-f\mathbf{u}_b\cdot\nabla_H\eta_b$ using the measured site bottom currents and topographic gradients (section 3), or as $\int_{\eta_b}^{0}fw_z dz$ using the depth integral of total horizontal velocity divergence (section 6).

Using the geostrophic or total (gradient flow) fields described above we also attempt to estimate terms expected to be relatively small, including the nonlinear contribution to the divergence term, ζw_z; vortex tilting; and dissipative and diffusive terms. For the tilting term, $\mathbf{u}_z\times\nabla_H w$, we use finite differencing of w_z (4) integrated from the surface. We calculate bottom frictional stress based on either a linear [*Gill*, 1968] or quadratic [*Arbic and Scott*, 2008] drag parameterization and mapped bottom velocity fields, and then compute torques by finite differencing. We approximate horizontal diffusion of vorticity by eddies below the cDrake array resolution using a harmonic eddy-diffusivity parameterization, $\kappa_e\nabla_H^2\langle\zeta\rangle$, with $\nabla_H^2\zeta$ from finite differencing of mapped $\nabla_H\zeta$. To achieve comparable levels of eddy diffusion to those produced by the biharmonic parameterization found in SOSE we would use a constant eddy diffusivity of $\kappa_e=200$ m s^{-1}.

We calculated wind stress curl over the LDA using satellite-based surface wind vectors. For 2007-2009 we obtained 0.25-degree gridded, 3-day averaged Level 3 wind vectors from SeaWinds on QuikScat from Remote Sensing Systems (RSS) at ftp://ftp.ssmi.com/qscat/qscat_wind_vectors_v04/. The QuikScat wind vectors are calculated using the Ku-2011 algorithm [*Ricciardulli and Wentz*, 2011]. For 2009-2011 we obtained ASCAT Level 2 swath data from JPL PODAAC at ftp://podaac-ftp.jpl.nasa.gov/allData/ascat/preview/L2/25km. ASCAT data are provided by the European Organisation for the Exploitation of Meteorological Satellites (EUMETSAT) and the Royal Netherlands Meteorological Institute (KNMI). We average both QuikScat and ASCAT data to the cDrake objective mapping grid using Gaussian-weighted averaging with a 50-km decorrelation length, and combine them to form one time series for the cDrake time period. We convert vector wind to wind stress using the drag coefficient parameterizations of *Yelland and Taylor* [1996, for speeds below 6 m s^{-1}] and *Yelland et al*. [1998, above 6 m s^{-1}]. Gradients are estimated by center differencing.

2.2. Shipboard ADCP

Shipboard acoustic Doppler current profiler (SADCP) velocity measurements in the top 1000 m of Drake Passage have been collected on approximately twice-monthly, all-season crossings by the ARSV Laurence M. Gould (LMG) since November 2004. The 183 crossings through October 2013 have been compiled into a mean velocity field on a 25-km by 25-km horizontal grid with 24-m vertical resolution [*Firing et al*., 2011; *Lenn et al*., 2007]. The LMG takes a variable path across Drake Passage, producing a sampling fan spanning 50 km (at the northern end) to 450 km (at the southern end) of along-stream distance. The most common track runs just to the west of the cDrake central line and has 92 to 171 crossings through each 25-km segment.

We use the time-mean gridded SADCP velocities to compute mean relative vorticity $\langle\zeta\rangle = \langle v\rangle_x - \langle u\rangle_y$ and mean relative vorticity advection $\langle\mathbf{u}\rangle \cdot \nabla_H\langle\zeta\rangle$ by center differencing. From SADCP data on the most common track, we compute a time series of one component of relative vorticity advection, $v_{tr}u_{tr,yy}$, where $(u, v)_{tr}$ are across- and along-track velocity and y_{tr} is the along-track coordinate, rotated approximately 9° from meridional. We compare this quantity to cDrake vu_{yy} computed from the 3-day low-pass filtered mapped data (neglecting the 9° difference in orientation).

The SADCP and cDrake fields represent quite different temporal and spatial scales, and we emphasize that the comparisons between them are intended to validate the statistics of the cDrake higher-derivative fields, rather than particular values at particular times or locations. The comparison of cDrake relative vorticity and vorticity gradients with those computed from this independent SADCP dataset by a different method is used to confirm that the cDrake objective mapping and GEM method does not result in over- or underestimation of the higher derivatives of velocity.

2.3. SOSE

We used numerical model output from the Southern Ocean State Estimate (SOSE) to examine the effect of horizontal resolution and coverage on the objective mapping results. The Southern Ocean State Estimate [*Mazloff et al*., 2010] is an eddy-permitting, data-assimilating state estimate which uses the adjoint method to iterate the MITgcm to minimize misfit between the estimate and observations by modifying model forcings (atmospheric fluxes and initial and boundary conditions) within their uncertainties. The model uses a $1/6°$ C-grid at 42 depth levels, with higher resolution near the surface. We use output from SOSE iteration 59, spanning 2005 through 2007 (data from cDrake are not assimilated into this version of SOSE). SOSE pressure anomalies were objectively mapped in the same manner as for the cDrake data, allowing us to map both from an LDA-like set of input points and from data extending beyond the edges of the mapping grid, producing better estimates of higher derivatives. We mapped to the cDrake LDA grid first from $1/6°$ fields extending 100 km beyond the grid, and secondly from fields from the LDA area sub-sampled to $1/3°$ (latitude) to $2/3°$ (longitude), or approximately 38 km (comparable to the cDrake LDA instrument spacing).

2.4. Satellite Altimetry

To extend the 4 years of cDrake results to a longer time period, we use satellite-derived mean absolute dynamic topography (MADT) produced by Ssalto/Duacs (http://www.aviso.oceanobs.com/en/data/product-information/duacs.html) and distributed by AVISO with support from CNES (http://www.cnes.fr). We use 21 years of the delayed-time MADT product, which incorporates sea level anomaly from multiple satellites (up to four at a time) with the CNES-CLS2013 mean dynamic topography. The fields are produced on a $1/4°$ grid by mapping with length scales of ~100 km [*Ducet et al*., 2000]. We compute surface geostrophic velocity, vorticity, and vorticity gradients from the sea surface height (the surface geostrophic stream function) both by finite differencing and by objective mapping (following the same method used for cDrake).

3. Flow Over Topography and Bottom Pressure Torque

The near-bottom currents measured by the cDrake array over 4 years (Figure 3a and *Chereskin et al*., 2012) are similar in magnitude, orientation, and variance to the first year of measurements discussed by *Chereskin et al*. [2009]. The mean currents (Figure 3a) at most sites throughout the passage flow nearly along the local topographic contours, with closer alignment where topographic gradients are stronger. This alignment of the flow along steep topography applies for topography smoothed at scales of 2 to 10 km, implying that these are the scales steering the flow at 50 m above the bottom. Time variability in current direction is small

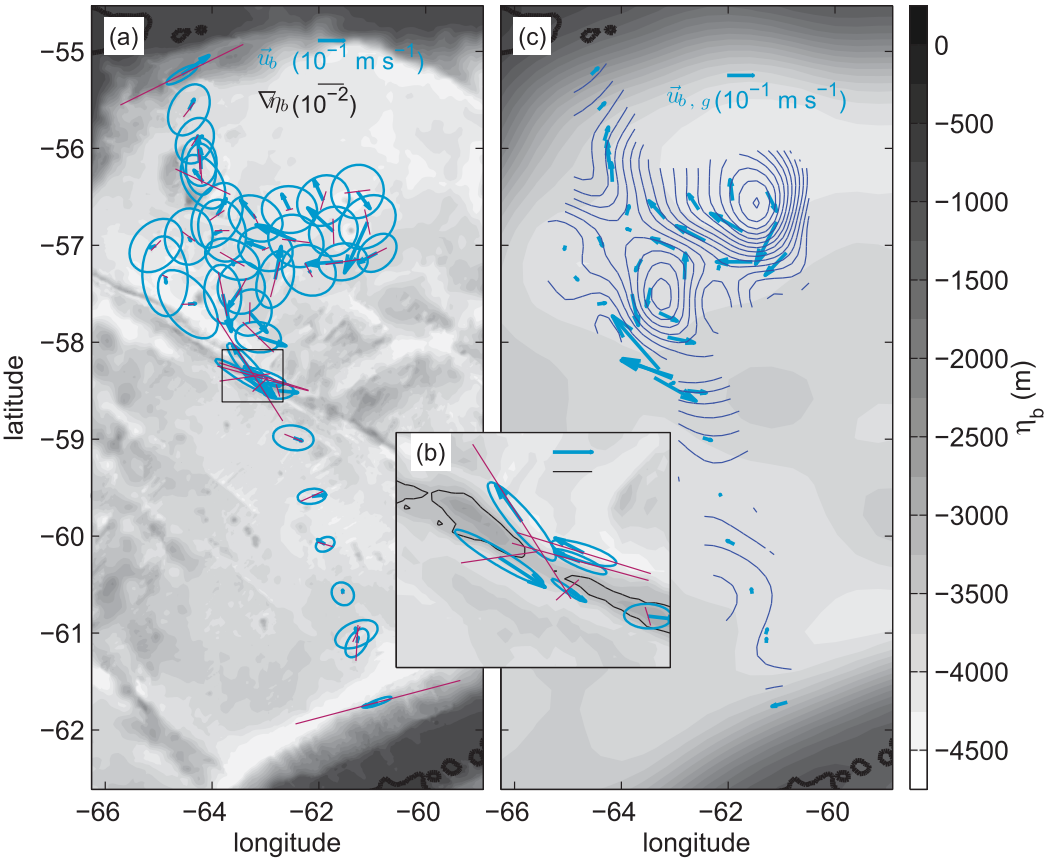

Figure 3. Bottom currents and topography: (a) mean vectors and standard deviation ellipses of measured near-bottom currents ($\mathbf{u}_b$, teal) and local (10-km-smoothed) isobath vectors (magenta, with length proportional to the bathymetry gradient magnitude), over the original bathymetry (gray scale filled contours, see section 2.1 and Figure 1); (b) inset showing the array over the SFZ, boxed area in Figure 3a, with the 3000 m isobath (black); scale vectors indicate the same magnitudes as those in Figure 3a; (c) mean bottom geostrophic stream function (blue contours, 0.2 $m^2\ s^{-2}$ interval) and geostrophic current vectors ($\mathbf{u}_{b,g}$, teal) over 50-km-smoothed bathymetry (gray scale filled contours).

over the SFZ (Figure 3b) and the northern and southern slopes (Figure 3a). In the eastern LDA, which lacks both major topographic features and local roughness, variance ellipses are close to isotropic.

Small deviations in mean current direction from exactly along the local topography produce downslope flow over the southern continental slope, and upslope flow over the northern slope (Figure 3a). Over the SFZ the CPIES measurements indicate a consistent pathway for the flow, with a preference for southeastward flow along the upstream (southwest) side of the ridge and northwestward flow along the downstream (northeast) side (Figure 3b). Some flow may be directed through a pass in the SFZ between the cDrake instruments (Figure 3b), but the mean flow at the instruments adjacent to and on the ridge implies a larger-scale diversion of the flow around this part of the ridge. Flow at the five SFZ CPIES adjacent to the pass is slightly down the local slope, on both sides of the ridge, while flow at the instrument atop the ridge south of the pass is more strongly upslope, so that the net vortex stretching due to flow over the SFZ appears to be small.

Objectively mapped geostrophic bottom current orientations (Figure 3c) are generally similar to the point-measurement total currents. Particularly in the LDA, where objectively mapped current direction is better-determined, differences in sign between $w_b = \mathbf{u}_b \cdot \nabla_H \eta_b$ and $\mathbf{u}_{b,g} \cdot \nabla_H \eta_b$, for a given η_b field, are associated with weak and/or nearly along-slope flows only. Time variability in these dot products is associated with variability in both current magnitude and direction, which is particularly strong between the SFZ and the northern slope (Figure 3a). In fact both time-mean and time-variable dot products are strongly sensitive to the current-topography angle, which itself is strongly sensitive to the smoothing scale chosen for the topography.

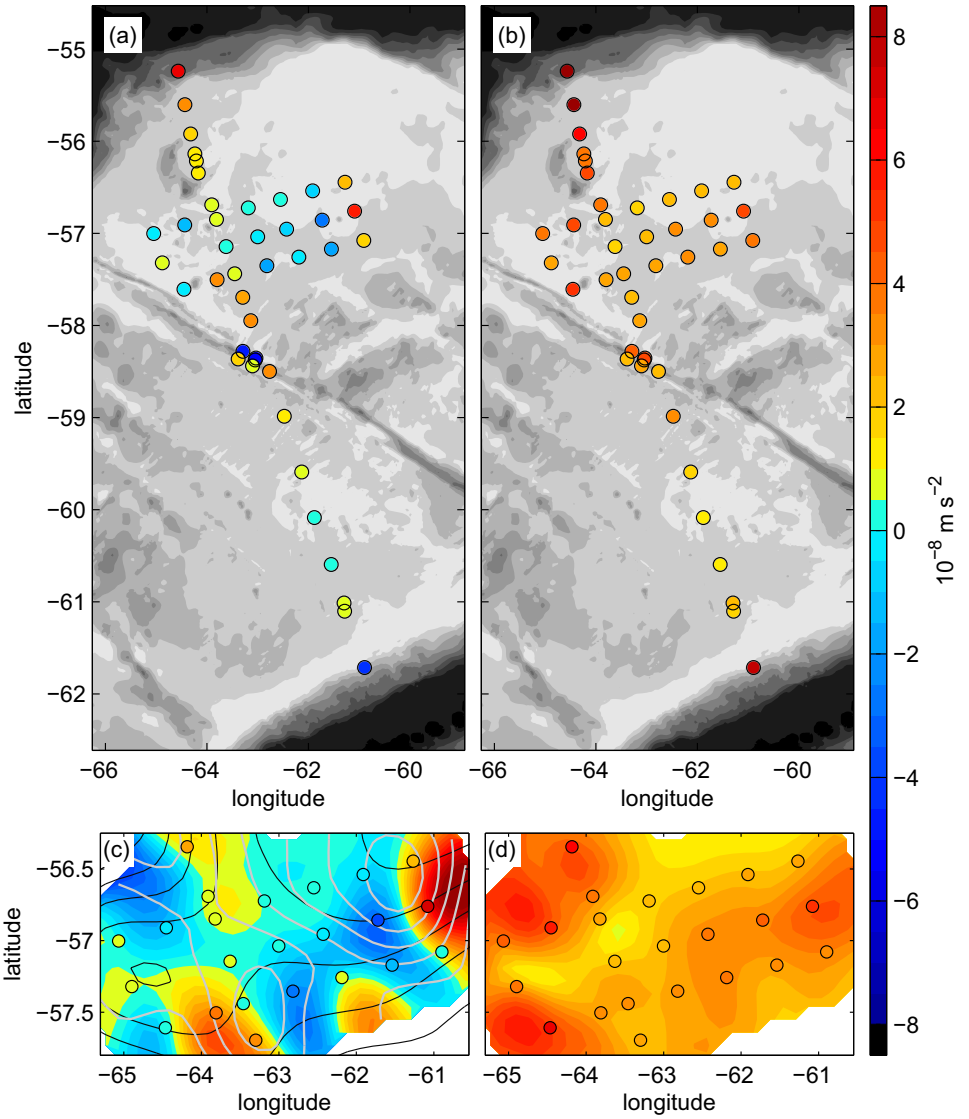

Figure 4. (a) Mean and (b) standard deviation from 7-day low-pass filtered time series of bottom pressure torque, $-J(p_b, \eta_b) = -f\mathbf{u}_{b,g} \cdot \nabla_H \eta_b$ at CPIES sites, estimated using mapped bottom geostrophic stream function and 50-km-smoothed topography (25-km for the sites over the SFZ). (c) Mean and (d) standard deviation in the LDA of mapped bottom pressure torque (filled color contours) and bottom flow over topography $-f\mathbf{u}_b \cdot \nabla_H \eta_b = -fw_b$ at CPIES sites (filled circles). The standard deviation exceeds the mean bottom pressure torque (or fw_b) at many points, but the standard error for these 4-year means is an order of magnitude smaller. Black contours in Figure 4c show the 50-km-smoothed η_b in the LDA (deepest in the bottom left and top right), and light gray contours the mean mapped bottom geostrophic stream function; note that the bottom geostrophic flow is upslope where bottom pressure torque is positive.

To estimate the bottom pressure torque forcing term in the mesoscale vorticity balance, we are interested in topography at scales that interact with the mesoscale bottom pressure field. Smoothing topography with a Gaussian with a 50-km length scale (Figure 3c) removes most of the topographic relief apart from the southern and northern slopes, including the SFZ. The mesoscale bottom pressure torques inferred from this topography (Figure 4) are large and positive over the northern slope (consistent with upslope flow, Figure 3c, and with possibly balancing βv for $v > 0$), and negative (but smaller) over the southern slope. Larger values in the LDA are due to the deep mean anticyclonic and cyclonic recirculations there, and thus nearly cancel out when averaged over 200-km scales. Positive bottom pressure torques on the upstream side of the SFZ and negative torques on the downstream side also cancel to first order, leaving a small positive residual. The mesoscale, 50-km flow may be affected by shorter-scale topography, as suggested by *Bishop et al.* [2012]. Bottom pressure torques computed using 25-km-smoothed topography are larger than those computed with 50-km-smoothed topography but otherwise similar in sign and distribution. Because the

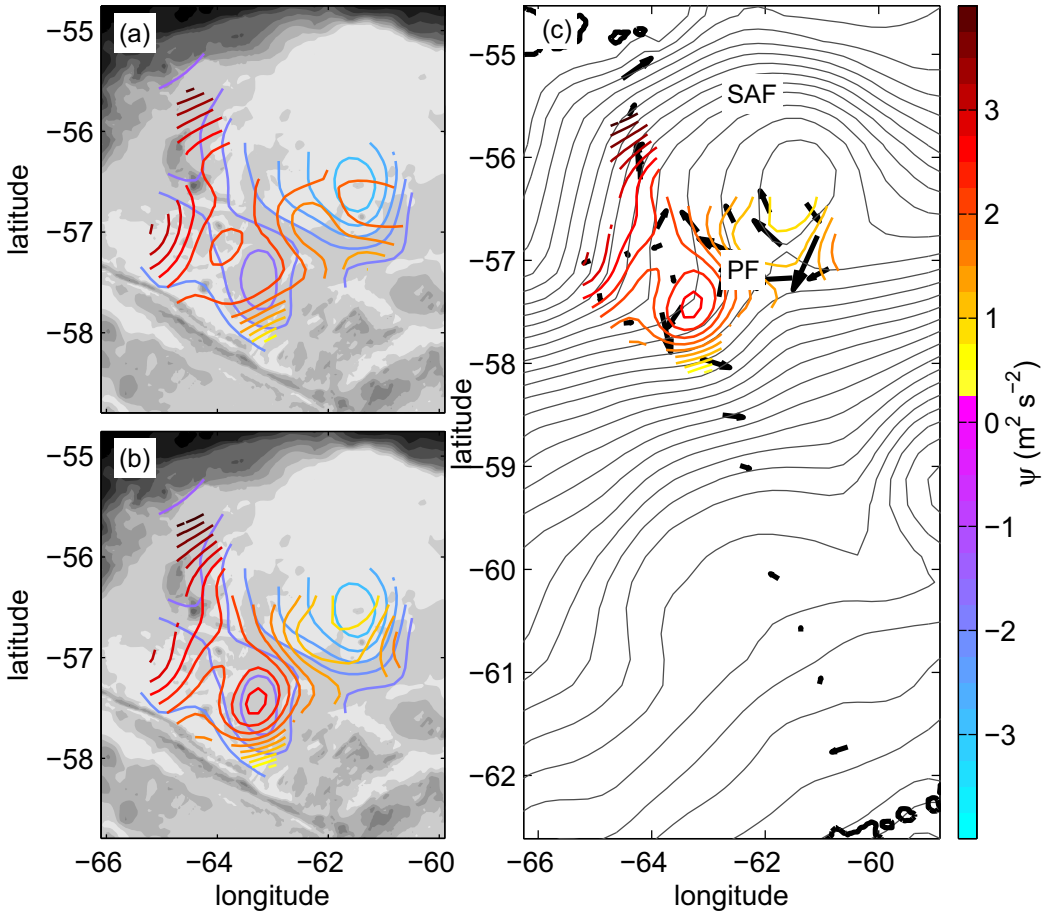

Figure 5. (a, b) Mapped cDrake time-mean barotropic geostrophic stream function (cool colors), (a) with baroclinic geostrophic stream function at 200 dbar (warm colors), (b) total geostrophic stream function at 200 dbar (warm colors), and bathymetry (gray); (c) cDrake total 200-dbar geostrophic stream function (warm colors) and surface MADT (gray) with cDrake 4000-dbar current vectors at CPIES sites (vector tails). Barotropic, baroclinic, and total cDrake geostrophic stream functions are contoured at intervals of 0.25 $m^2\ s^{-2}$ (each with arbitrary mean). MADT contours are every 5 cm (0.5 $m^2\ s^{-2}$). Bathymetric contour intervals are every 500 m from 4500 to 0 m. cDrake geostrophic stream functions are only shown where the objective mapping percent error of 3-day low-pass filtered maps is less than 30%.

mapped $\mathbf{u}_{b.g}$ differ slightly from the measured u_b, for the same topography, time-mean differences between the bottom pressure torque (Figure 4c filled contours) and flow over topography computed using total observed near-bottom currents (Figure 4c dots) are noticeable at a few points, in particular on the edges of the LDA; however, these differences produce little net effect. Time variability and the higher variance (Figure 4d) of fw_b compared to bottom pressure torque will be discussed in section 6.

The net bottom pressure torque integrated across the passage is approximately 4×10^{-3} to 6×10^{-3} $m^2\ s^{-2}$ (for 25 or 50 km smoothed bathymetry gradients, respectively). This corresponds to an average value of 3 to 4×10^{-9} $m\ s^{-2}$, or 15–20 times the mean wind stress curl.

4. Vertical Structure of Currents and Mapped Geostrophic Stream Function From cDrake

This section transitions from the near-bottom flow into the full water column, beginning in northern Drake Passage where the cDrake LDA was situated. The LDA (Figure 1) is located in the region of enhanced variability between the mean Subantarctic Front (SAF) and Polar Front (PF) positions (based on either climatological hydrography [*Orsi et al.*, 1995], or satellite sea surface height contour gradients, Figure 5). The barotropic (bottom reference) and baroclinic components of the depth-mean velocity have approximately equal variance, consistent with findings on barotropic and baroclinic contributions to Drake Passage transport variability by *Cunningham et al.* [2003] and *Firing et al.* [2011]. Typical median values for deep and

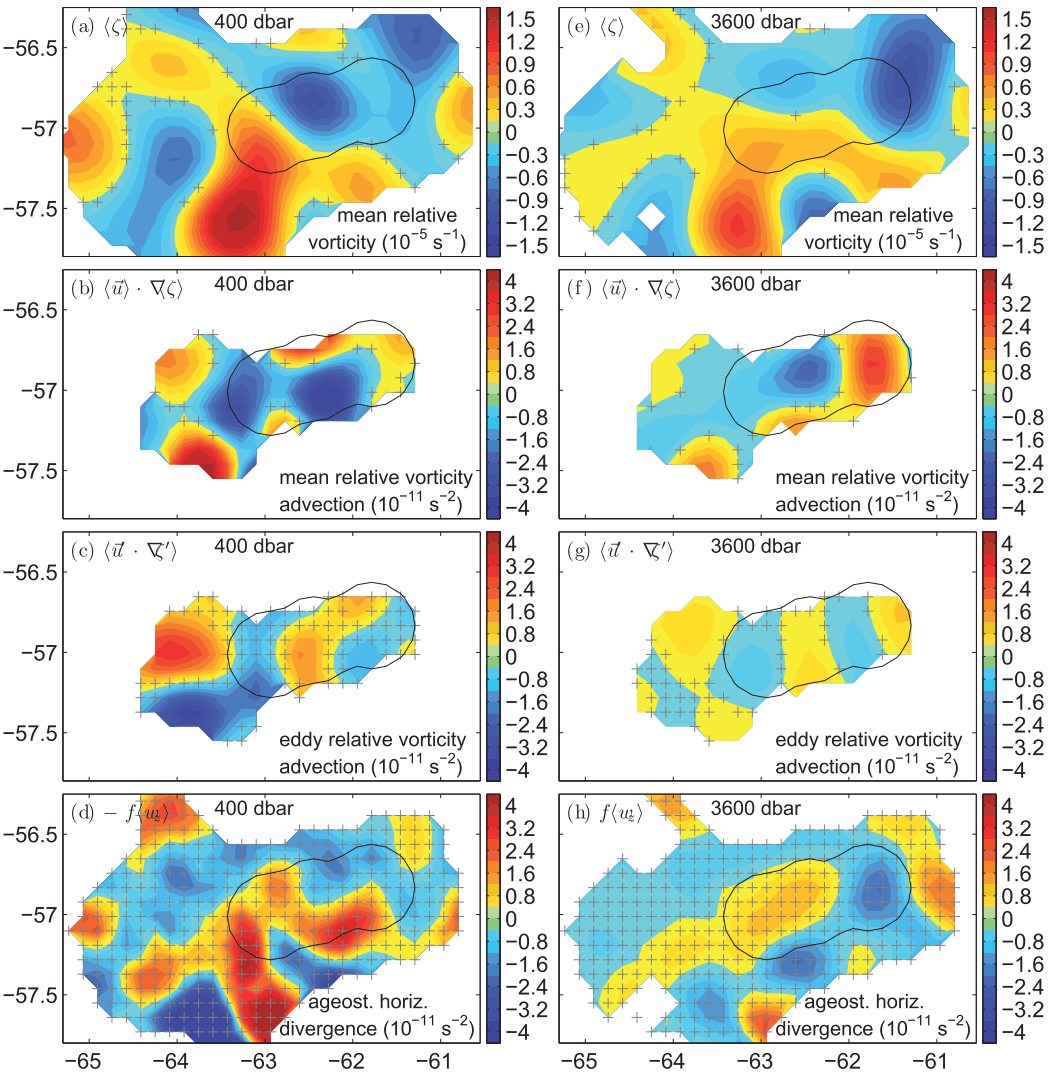

Figure 6. (a, e) Four year mean relative vorticity $\langle\zeta\rangle$, (b, f) mean relative vorticity advection $\langle\mathbf{u}\rangle \cdot \nabla_H\langle\zeta\rangle$, (c, g) eddy relative vorticity advection $\langle\mathbf{u}' \cdot \nabla_H\zeta'\rangle$, and (d, h) ageostrophic stretching $f\langle w_z\rangle$ at (a–d) 400 dbar and (e–h) 3600 dbar in the LDA. Points with values smaller than their uncertainties are covered by gray pluses (see text for discussion of possible overestimation of uncertainties on ageostrophic quantities, included in Figures 6d and 6h). The thin black line outlines the area from which the time series in Figure 8 are averaged.

shallow 7-day low-pass filtered, objectively mapped speed in the LDA are 10 and 30 cm s^{-1}, respectively [*Firing et al.*, 2014, Figure 7], while RMS errors over the LDA are 4–13 cm s^{-1}; errors decrease with depth and increase with distance from the LDA [*Firing et al.*, 2014, Figure 7]. The cDrake velocity fields in the LDA are dominated by meander and eddy events like the one discussed in *Chereskin et al.* [2009, Figure 4], where a southeastward meander of the SAF and a northward meander of the PF led to the development of an anticyclonic and cyclonic eddy, respectively, in the LDA area. During these events, which occur about 5 times a year over the 4-year record, near-bottom daily-mean speeds can exceed 40 cm s^{-1} for time intervals of approximately a week.

Different events have different paths of development through the array, but averaged over 4 years, the net result of the LDA meander/eddy events in the deep flow is an anticyclonic circulation (meander crest) in the area just downstream of the SFZ, and a stronger cyclonic circulation (meander trough) in the Yaghan Basin (Figures 5a and 5b). The mean deep flow appears to be deflected around some of the seamounts in the northwestern part of the array, but the northeastward flow of the SAF is otherwise visible in the deep streamlines at the northern end of the LDA. The mean 200-dbar baroclinic streamlines (Figure 5a) capture parts of the SAF and PF jets at the northwestern-northern and southern edges, respectively, of the mapping

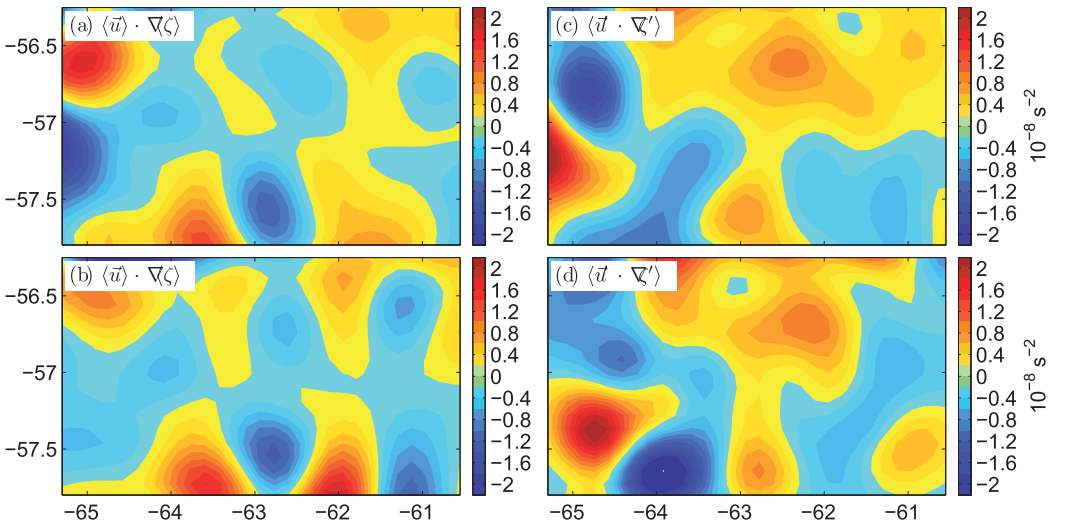

Figure 7. (a, b) Four year mean relative vorticity advection $\langle \mathbf{u} \rangle \cdot \nabla_H \langle \zeta \rangle$ and (c, d) eddy relative vorticity advection $\langle \mathbf{u}' \cdot \nabla_H \zeta' \rangle$ at 380 m, mapped from SOSE pressure anomaly fields from (a, c) extended and (b, d) limited input points (see text).

area. The baroclinic flow also features a northward meander trough centered at 57°S, 62.5°W (to the southwest of the deep cyclonic eddy) and a southward meander crest with a small closed anticyclonic contour at 57°S, 64°W (slightly to the northwest of the deep anticyclonic eddy).

The mean baroclinic (relative to the bottom) and barotropic (deep reference) geostrophic stream functions (Figure 5a) are rarely parallel. Recalling that, as illustrated in Figure 2, the extent of turning with depth depends on both the relative angles and relative sizes of the barotropic and baroclinic components, we look for net turning with depth of the total current of $\mathcal{O}(1)$ rad (corresponding to significant w [*Hughes and Killworth*, 1995]) as an indicator of non-equivalent-barotropic flow. On the very eastern edge of the array, for example, although the barotropic and baroclinic streamlines cross, the total 200-dbar streamlines (the sum of the barotropic and baroclinic components) are nearly aligned with the deep streamlines (Figure 5b), and turning with depth is small. The areas with the largest turning with depth tend to be those with a larger baroclinic contribution. The angle change between the 200-dbar total current and the bottom (barotropic) current is greater than 0.5 rad over about half the LDA area, including the relatively flat central and eastern LDA. In the northwestern corner of the array the weak bottom currents may be steered around the Yaghan seamounts; the western side as a whole may be influenced by the SFZ just upstream. Following the geostrophic streamlines across the array from west to east (Figure 5b), the sign of the rotation switches from cyclonic with increasing depth (veering) heading into the meander crest (high/anticyclonic circulation) to anticyclonic with increasing depth (backing) between the crest and trough, and back to cyclonic at the downstream side of the trough, as described in the Gulf Stream by *Lindstrom et al*. [1997] and elsewhere in the time-varying ACC by *Tracey et al*. [2006], *Phillips and Rintoul* [2000], and *Phillips and Bindoff* [2014]. The associated vertical velocities—downwelling between the eastern side of the meander crest and the middle of the trough, and upwelling on the western side of the meander crest and eastern side of the trough—are also consistent with those predicted from the direction of the observed near-bottom flow relative to topography (Figure 4c).

Outside the two-dimensional LDA, the baroclinic current direction cannot be determined from the cDrake data, so we use satellite-derived mapped absolute dynamic topography (MADT), averaged over the cDrake time period, to compute the surface current direction. The MADT geostrophic stream function (Figure 5c) parallels the cDrake total geostrophic stream function at 200 dbar in the orientation and curvature of the SAF, on the western and northern sides of the LDA, as well as the part of the mean PF captured by the LDA. The large cyclonic circulation visible in the eastern LDA is also present in the MADT, although with smaller amplitude. The MADT does not show the anticyclonic recirculation visible in the southwestern LDA in both the barotropic reference and total near-surface cDrake geostrophic stream functions (Figure 5b); this feature may be below the effective resolution of the satellite maps, which use length scales around 100 km [*Ducet*

et al., 2000]. MADT surface streamlines (representing the total geostrophic surface current) and cDrake bottom current vectors (Figure 5c) are aligned in the northern part of the SAF, but by its southern edge they are rotated by about 0.5 rad. Similarly, in the PF surface and deep current angles differ by 0.5–0.6 rad, while south of the PF some near-bottom currents oppose the surface current. In the SAF and PF south of the LDA, where the one-dimensional part of the array does not allow for geostrophic mapping as accurately as in the LDA, the near-bottom current directions are nevertheless consistent between current meters, implying that they are likely to represent the mesoscale deep flow direction and its rotation from the surface flow.

5. Relative Vorticity and Its Advection in the LDA

The two-dimensional horizontal coverage in the LDA allows us to compute higher derivatives of geostrophic stream function, the relative vorticity and relative vorticity gradient fields (Figure 6). Mapped relative vorticity, which has typical 7-day low-pass filtered amplitudes of 4×10^{-5} s^{-1} at 400 dbar and 1.5×10^{-5} s^{-1} at 3600 dbar [see *Firing et al*., 2014, Figure 7], has errors about 20% of its amplitude. Relative vorticity gradient errors are 2×10^{-10} to 4×10^{-10} m^{-1} s^{-1} within the LDA, about half the typical gradient amplitude. Uncertainties on 4-year time mean fields are approximately 10 times smaller (based on the 11-day estimated decorrelation time scale for the LDA observations) [*Firing et al*., 2014]. The ageostrophic mean and eddy relative vorticity advections (not shown) mirror the spatial patterns of the geostrophic terms, and are 10–20% the size; overall they tend to reduce the total vorticity advection, in particular at depth.

Chereskin et al. [2009] described two eddy events in the LDA where the Rossby number $Ro=\zeta/f$ from daily-mean near-bottom current measurements was at least ±0.15. In 4 years of 7-day low-pass filtered mapped vorticity we find several such events each year. At 200 dbar $|Ro| \geq 0.2$ occurs 12% of the time and $|Ro| \geq 0.1$ occurs 40% of the time (with a maximum magnitude of 0.75), while at the bottom $|Ro| \geq 0.1$ occurs 6% of the time (with a maximum of 0.35). Both relative vorticity and relative vorticity advection are highly variable in time, with standard deviations of 10^{-5} s^{-1} and 10^{-11} s^{-2}, respectively. There is a slight (55%–65%) preference for negative (cyclonic) ζ, more pronounced in the deep than in the shallow currents. Relative vorticity and relative vorticity advection decrease by on average a factor of two to three between 400 and 3600 dbar over most of the LDA, although in the persistent Yaghan Basin deep cyclone (in the northeastern corner of the array), velocity and vorticity both increase with depth [see also *Firing et al*., 2014]. Although relative vorticity advection changes sign between the near-surface and near-bottom approximately 36% of the time, the decrease in magnitude with depth limits cancellation in the depth integral. Thus, the upper flow in general gives a qualitatively correct picture of full-column vorticity advection.

The mean relative vorticity in the LDA (Figure 6) is approximately 10^{-5} s^{-1} (giving $Ro=\mathcal{O}(0.1)$) and reflects the standing eddies visible in the mean streamlines (Figure 5) and the dipole pattern found in satellite sea level anomaly by *Ferrari et al*. [2012]. The mean vorticity field decreases only slightly with depth, and shallow and deep fields are correlated ($r = 0.76$ between 400 and 3600 dbar, significant at the 99% level). The cDrake time series also allows us to separate out the mean relative vorticity advection, $\langle\mathbf{u}\rangle \cdot \nabla_H\langle\zeta\rangle$, from the eddy relative vorticity advection, $\langle\mathbf{u}' \cdot \nabla_H\zeta'\rangle$, where the angle brackets represent the mean over 4 years. Mean and eddy relative vorticity advection are $\mathcal{O}(10^{-11})$ s^{-2}, with the mean contribution about twice as big as the eddy contribution. Each component ($u\zeta_x$ and $v\zeta_y$) of eddy relative vorticity advection is larger than the corresponding mean component, but the eddy components are also more negatively correlated with each other. Both relative vorticity advection constituents (Figure 6) show some correlation with depth ($r=0.55, 0.44$ between 400 and 3600 dbar for mean and eddy, respectively, both significant at the 99% level based on a 50-km decorrelation length scale), with mean advection magnitude decreasing by a factor of two from 400 to 3600 dbar, and eddy advection magnitude by a factor of three. Planetary vorticity advection (not shown) has a slightly more barotropic depth profile.

5.1. Relative Vorticity and Vorticity Advection From SADCP Velocity

The long-term SADCP dataset provides an independent check on the size of the mean and eddy relative vorticity advection terms in Drake Passage. We compare RMS values of cDrake mapped fields with RMS values of the same fields estimated from the SADCP velocity measurements in the LDA area (Table 1). The cDrake and SADCP RMS $\langle\zeta\rangle$ are consistent (to within a factor of 2) and both decrease near-linearly with depth over the top 1000 m. The mean relative vorticity advection, $\langle\mathbf{u}\rangle \cdot \nabla_H\langle\zeta\rangle$, also decreases near-linearly with depth. The RMS values of the SADCP and cDrake track-resolvable mean relative vorticity advection

Table 1. Relative Vorticity and Relative Vorticity Advection Components From cDrake and SADCP in the LDA[a]

	$\langle\zeta\rangle$ (10^{-6} s^{-1})		$\langle\mathbf{u}\rangle \cdot \nabla_H\langle\zeta\rangle$ (10^{-11} s^{-2})		$\langle v\rangle\langle u_{yy}\rangle$ (10^{-11} s^{-2})		$\langle v'u'_{yy}\rangle$ (10^{-11} s^{-2})	
	100 m	1000 m	100 m	1000 m	100 m	1000 m	100 m	1000 m
cDrake	5.6	4.4	2.5	1.5	1.8	1.0	2.1	0.8
SADCP	4.2	2.7	2.8	1.6	1.5	0.8	1.9	0.4

[a]RMS values at 100 and 1000 m depth.

component ($\langle v\rangle\langle u_{yy}\rangle$) in the overlap area of the LDA and the most common LMG track (Figure 1) are approximately the same size, with the SADCP values decreasing slightly faster with depth. The RMS cDrake track-resolvable eddy component ($\langle v'u'_{yy}\rangle$) decreases faster with depth than the same quantity from SADCP, but is still within a factor of two. Both SADCP and cDrake have mean and eddy components of similar size, and a faster decrease with depth in the eddy components than in the mean.

Given the differences between cDrake and SADCP sampling (daily, 7-day low-pass filtered time series from 2007 to 2011, versus approximately twice-monthly synoptic data from 2004 to 2013) and spatial smoothing (center differencing the 25-km SADCP grid produces an effective length of 75 km, compared to the cDrake 50-km high-pass mapping scale), the agreement between cDrake and SADCP vorticity and vorticity advection components is remarkably good; the RMS values of the SADCP estimates are within a factor of two of the cDrake RMS values, and the depth structures and relative sizes of mean relative vorticity advection and the resolvable component of eddy relative vorticity advection are reproduced. Thus, the SADCP data appear to support the conclusion from the simulations described in Firing et al. [2014] that we can accurately map both mean and time-varying vorticity and vorticity gradients (and therefore vorticity advection) in the LDA.

5.2. Mapped Relative Vorticity Advection From SOSE

To compare with the observed vorticity balance terms from cDrake, and to check the robustness of the mapped derivatives, we objectively mapped SOSE 5-day-averaged pressure anomaly fields, using the same methods and parameters as for the cDrake LDA. We mapped either from points in the LDA area alone or from an extended area (100 km beyond the edges of the mapping area), and either from the full 10–20 km SOSE resolution or from fields subsampled to ~40 km (approximately the cDrake LDA instrument spacing). Differences between the resulting mapped relative vorticity advection fields are small except on the boundaries of the mapping area (Figure 7). The SOSE fields are lower in energy than the observations; SOSE relative vorticity advection is about half the size for the same mapping scales (compare to Figure 6). Mean and eddy relative vorticity advection, which tend to oppose each other in SOSE, are also closer to the same size in SOSE than in cDrake, and mean relative vorticity advection diminishes more quickly with depth in SOSE than in the observations. Despite these differences, the maps from SOSE help confirm that relative vorticity gradients and relative vorticity advection can be successfully estimated from a limited cDrake-like set of input points sampling an eddying field.

6. Vorticity Balance in the LDA

Although nonlinear relative vorticity advection (Figures 6b, 6c, 6f, and 6g) decreases more quickly with depth than the linear planetary vorticity advection (not shown), βv remains an order of magnitude smaller at every depth. With $f \gg \zeta$ (Figures 6a and 6e), the time-mean stretching term is correspondingly dominated by the contribution of the divergence of ageostrophic velocity to fw_z (Figures 6d and 6h).

To examine the time-varying and depth-varying vorticity balance we focus on an approximately 130 km by 60 km area in the eastern LDA (see Figure 6), where 4-year records of sound travel time, bottom pressure, and near-bottom currents are available on all sides and thus uncertainties are smallest. Averaging over the whole LDA reduces the magnitude of all terms relative to averaging over this smaller area, but otherwise produces the same qualitative results (not shown).

As planetary advection (Figure 8, magenta), wind stress curl (not shown), nonlinear divergence (not shown), and tilting (not shown) are small, the first-order balance for relative vorticity advection (teal) is provided by the ageostrophic divergence ($fw_{a,z}$, gray). These two terms are negatively correlated, with $r = -0.60$ near

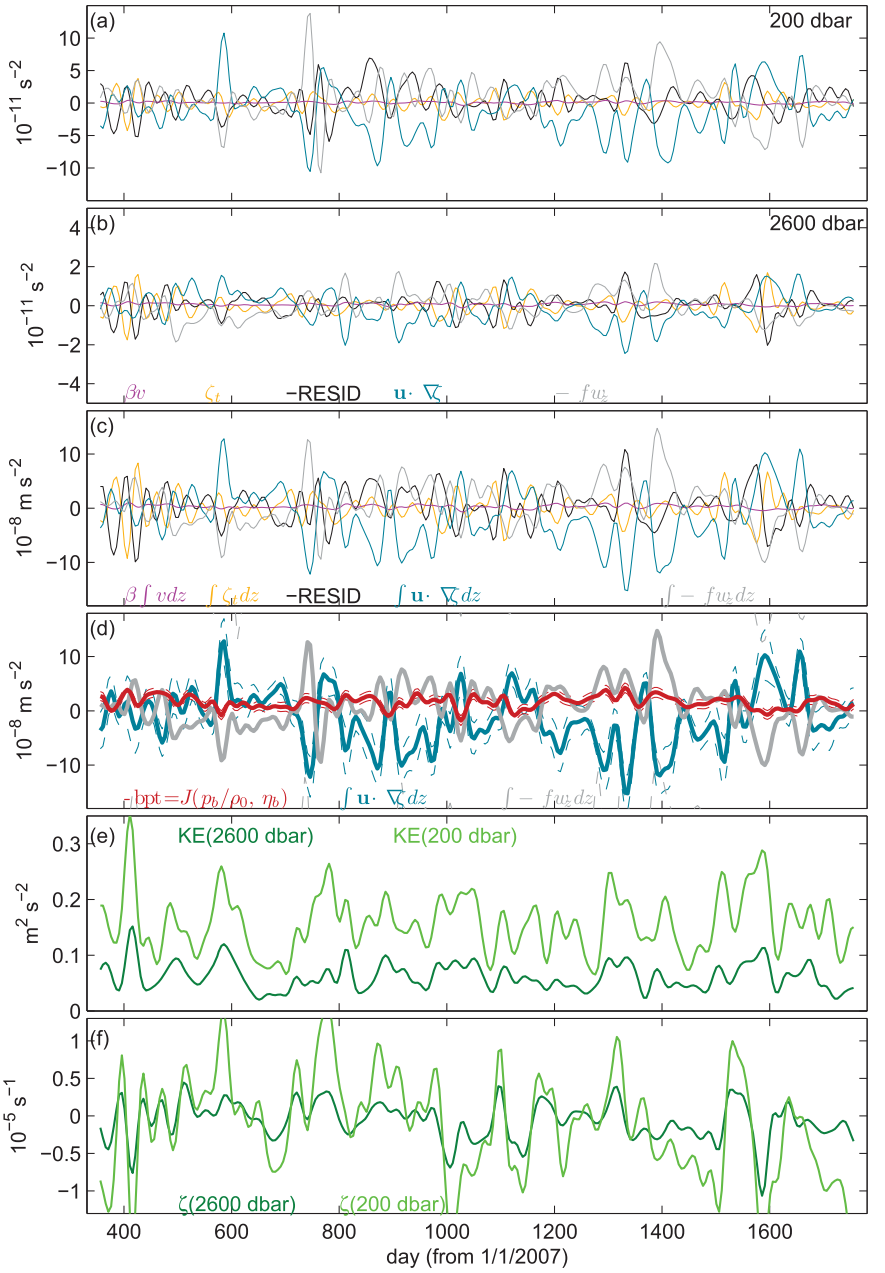

Figure 8. Time series from the central-eastern LDA of 30-day low-pass filtered cDrake planetary vorticity advection (magenta), vorticity tendency (gold), relative vorticity advection (teal), negative stretching (gray), and the negative of their residual (black) at (a) 200 dbar and (b) 2600 dbar. (c) The depth integrals of these quantities. (d) The time series of the dominant terms, depth-integrated relative vorticity advection (teal) and negative stretching (gray), are repeated along with that of negative bottom pressure torque (red), with uncertainties indicated by dashed lines. (e) Time series of shallow and deep kinetic energy and (f) relative vorticity are also shown. All time series are averaged over grid points in the central-eastern LDA area outlined on Figures 1, 6, and 9.

the surface, increasing to $r=-0.85$ at 4000 dbar. At time scales up to 60 days, the vorticity tendency (gold) is also intermittently first order. A first-order residual at these time scales (e.g., the 30-day low-pass time series in Figure 8) is produced in some cases by a mismatch in the sizes of advection and divergence peaks, and in some cases by the vorticity tendency, which does not appear to be balanced by any of the other terms. At longer time scales the tendency term, and the depth-varying residual, become second order or smaller.

As in the model results of *Thompson and Naveira Garabato* [2014], the relative sizes of relative vorticity advection and divergence change with depth, with time-varying divergence approximately 15% smaller

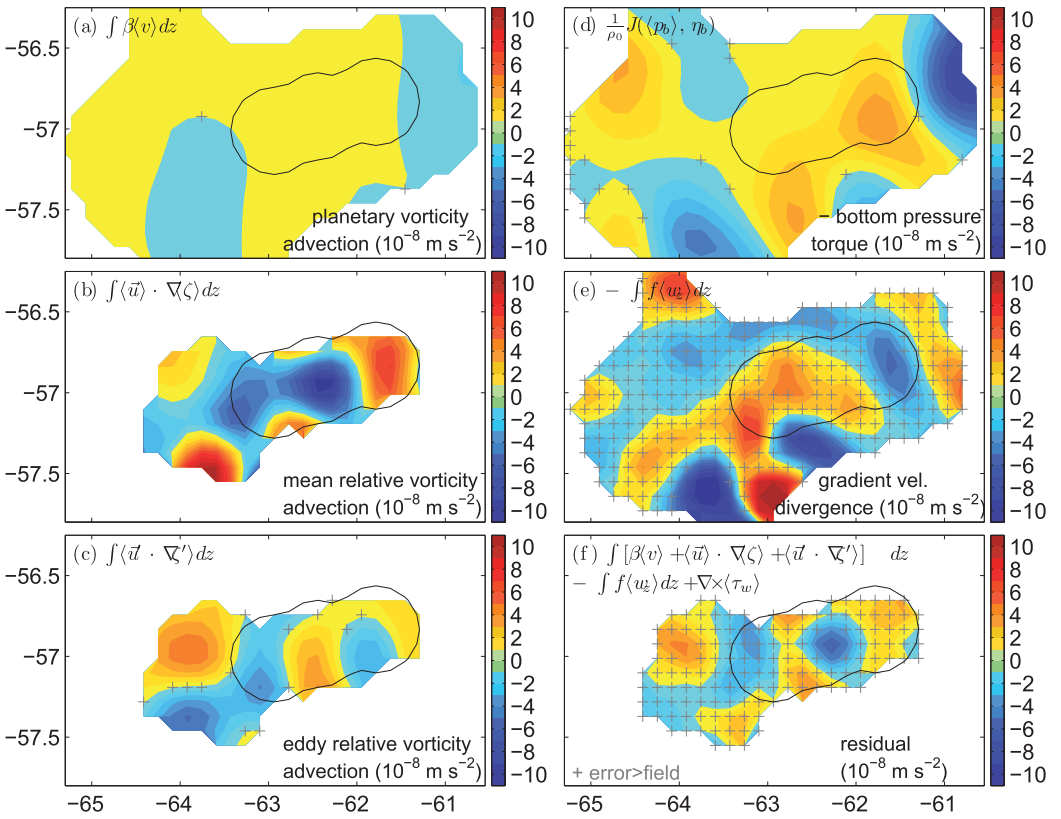

Figure 9. Selected terms of the depth-integrated mean vorticity balance: (a) planetary vorticity advection, (b) mean relative vorticity advection, (c) eddy relative vorticity advection, (d) the negative of bottom pressure torque, (e) the negative vortex stretching term including both geostrophic (Figure 9d) and ageostrophic contributions, and (f) the residual of Figures 9a–9c and 9e, and wind stress curl (not shown). Points smaller than the standard error of the mean are covered by gray pluses (see text for discussion of possible overestimation of uncertainties on ageostrophic quantities, affecting Figures 9e and 9f).

near the surface (Figure 8a), of the same size in midcolumn (Figure 8b), and approximately 10% larger at depth. In contrast, the spatial variance of the 4-year-mean relative vorticity advection (the sum of the mean and eddy components, Figures 6b, 6c, 6f, and 6g) is slightly larger than that of the divergence of gradient flow term (dominated by the ageostrophic contribution, Figures 6d and 6h) throughout the water column.

Depth-integrated divergence and relative vorticity advection (Figures 8c and 8d) are also well correlated ($r = -0.8$), with advection being larger in most events. Although bottom pressure torque is weakly negatively correlated with relative vorticity advection (Figure 8d) and tends to be positive while relative vorticity advection tends to be negative, the time variability in bottom pressure torque is only about one-quarter the size of that in total depth-integrated divergence (or relative vorticity advection) at weekly to multimonth time scales. Both kinetic energy peaks (Figure 8e) and peaks in relative vorticity advection amplitude (Figure 8d) lasting between 60 and 100 days stand out in the time series; however, the magnitude of the depth-integrated nonlinear vorticity advection shows only weak relationships to shallow or deep kinetic energy (Figure 8e, $r = 0.3$), or shallow or deep vorticity (Figure 8f, $|r| < 0.2$), over time.

Selected terms from the depth-integrated time-mean quasi-geostrophic vorticity balance in the LDA are shown in Figure 9. The dominant terms are the mean relative vorticity advection (Figure 9b) and the depth-integrated ageostrophic horizontal divergence; bottom pressure torque (Figure 9d) is only about one-third the size of the total depth-integrated divergence (Figure 9e) in the time mean, while eddy advection (Figure 9c) over 4 years is, as noted above, about half the size of mean advection. Planetary vorticity advection (Figure 9a) is a tenth the size of the nonlinear term, and local wind stress curl (not shown) is even smaller. The time-mean bottom frictional torque based on near-bottom mapped currents and either linear or quadratic flat-bottom drag parameterizations (not shown) is 4 orders of magnitude smaller than mean bottom pressure torque. The nonlinear contribution to the divergence term (ζw_z, not shown) and the tilting term

($\mathbf{u}_z \times \nabla_H w$, not shown) are both confirmed to be second order, comparable to βv. A harmonic parameterization for vorticity diffusion due to sub-mapping-scale eddies (not shown), using a large diffusivity of $\kappa = 200$ m s^{-1}, is the same size as the eddy relative vorticity advection, but its spatial pattern is uncorrelated with any of the other terms in the balance, or their residual. Total (mean and eddy) relative vorticity advection and total horizontal velocity divergence are well correlated ($r = 0.9$), leaving a residual (Figure 9f) of comparable size to the eddy advection or bottom pressure torque terms. We note that the uncertainties used for the residual in Figure 9f include the likely-overestimated finite-differencing uncertainty on the ageostrophic gradients (section 2). The discrepancy between the depth-integrated divergence and bottom pressure torque (given the negligible bottom frictional torque or bottom Ekman velocity), meanwhile, reflects both uncertainties in the velocity and velocity divergence fields and uncertainties in the scales of topography relevant for producing bottom pressure torque.

7. Discussion

7.1. Local Vorticity Balance in the PFZ in Drake Passage

The time-varying and time-mean local vorticity balances in the PFZ are dominated by mean relative vorticity advection and horizontal velocity divergence, including significant ageostrophic contributions. The magnitude of nonlinear vorticity advection has only a weak correlation with local eddy kinetic energy over time, in contrast to the association between elevated nonlinear vorticity advection and high eddy kinetic energy or meander strength in the model results of *Thompson and Naveira Garabato* [2014]. The residual of the terms in the quasi-geostrophic vorticity budget is first order, as none of the other terms (geostrophic planetary vorticity advection, bottom pressure torque, and wind stress curl) is large enough to balance the mean relative vorticity advection. Considering cyclostrophic dynamics by estimating gradient flow from the geostrophic maps and including its contribution to vorticity advection and particularly to ageostrophic divergence decreases the residual to one-third to one-half the size of the dominant terms. The cDrake observations confirm the first-order balance between nonlinear relative vorticity advection and predominantly ageostrophic stretching that *Thompson and Naveira Garabato* [2014] found in both the time-varying and time-mean balances at scales of tens of kilometers in an eddy-resolving model.

The vorticity balance terms and uncertainties computed by the objective mapping procedure used here have been validated by *Firing et al.* [2014] as well as by comparison with SADCP-derived vorticity advection and SOSE modeled vorticity balance terms (sections 5.1 and 5.2). Objective mapping of SOSE pressure anomaly fields in the same manner as the cDrake pressure or geopotential anomaly fields, from input points over a larger area to decrease uncertainties on higher derivatives, produces fields that agree qualitatively with the cDrake fields in the LDA.

The 4-year-mean cDrake vorticity balance residual has a small negative correlation ($r = -0.3$) with both bottom relative vorticity ζ_b and with $|\mathbf{u}_b|\zeta_b$, consistent with a contribution from the curl of bottom (frictional) drag parameterized as the quadratic $|\mathbf{u}_b|\mathbf{u}_b$. While standard flat-bottom drag parameterizations are orders of magnitude smaller than necessary to explain the residual (section 6), the seafloor in the LDA features rough topography at a range of scales, raising the possibility of enhanced drag on the deep geostrophic currents (and corresponding dissipation of vorticity) through internal wave generation by the geostrophic flow over topography [*Nikurashin and Ferrari*, 2010a, 2010b], as suggested by *Thompson and Naveira Garabato* [2014].

In the central-eastern LDA, where we have examined the time-varying local vorticity balance (Figure 8), variations in vorticity over time are relatively small (standard deviation of 2×10^{-6} s^{-1}, about half the size of the spatial standard deviation of the time-mean relative vorticity). The dominant terms of the balance, relative vorticity advection and ageostrophic divergence, as well as the residual of computed terms, are not strongly correlated with deep eddy kinetic energy or vorticity. Although the mean bottom pressure torque in this area is larger than the mean depth-integrated ageostrophic divergence (-2×10^{-8} s^{-1} for bottom pressure torque and -1×10^{-8} s^{-1} for ageostrophic divergence), the ageostrophic contribution to the time-varying balance is several times larger than the bottom pressure torque contribution (standard deviations of 4×10^{-8} and 1×10^{-8} s^{-1}, respectively). The time-varying residual in this region is most strongly correlated ($r = 0.5$) with near-bottom cross-slope current speed (not shown; the cross-slope direction is defined at the 25- to 50-km scale). In addition to being associated with increased wave-mediated bottom drag,

strong bottom currents might also be expected to be associated with increased contributions to advective, divergent, and/or diffusive terms by other smaller scale, ageostrophic motions not resolved by either the GEM and geostrophic mapping method or by including cyclostrophic dynamics, such as bottom-trapped topographic Rossby waves generated by strong cross-isobath flow. However, the low correlations with the residual make it difficult to identify which if any of these neglected terms might be important in the local vorticity balance.

7.2. Vertical Structure and the Vorticity Balance

The cDrake time-mean velocity fields deviate substantially from an equivalent-barotropic vertical structure over at least half of the LDA (section 4, Figure 5b), with rotations consistent with the meander dynamics described by *Lindstrom et al*. [1997], *Phillips and Rintoul* [2000], *Tracey et al*. [2006], and *Phillips and Bindoff* [2014]. While the mean currents in SOSE tend to exhibit less rotation in the jet centers and in regions of low topographic relief [*Peña-Molino et al*., 2014], cDrake bottom currents are significantly rotated from surface currents throughout the nonmeandering segment of the PF [*Foppert et al*., 2016], as well as flat parts of the array. Mean near-bottom currents over much of the rest of Drake Passage are also rotated 0.5 rad or more from the MADT-derived surface current direction (Figure 5c), and this rotation is not limited to the near-bottom fields, but is present in the profiles of combined baroclinic plus bottom reference objectively mapped geostrophic current (not shown). The extent of turning in the current profiles, even on the eastern side of the LDA (200 km downstream of the SFZ and 160 km downstream of the small-lateral-scale seamounts in the northwestern LDA) and in southern Drake Passage (200 km downstream of the Phoenix Ridge), implies that the departure from equivalent-barotropic vertical structure in the time mean persists at least that far downstream of topography. The cDrake data indicate that the full-depth ACC in Drake Passage is equivalent-barotropic only in the northern part of the SAF, where flow is strongly directed along the steep topographic slope.

The mean currents 50 m above the bottom are steered by local (scales up to 10 km) topography, even in areas of relatively low topographic relief such as the central and eastern LDA and the sites between the SFZ and the Antarctic continental slope, where the bottom depths range from 3500 to 4300 m. Bottom pressure torque, meanwhile, is produced by the interaction between the mesoscale geostrophic flow and topography. The size discrepancy between depth-integrated divergence and bottom pressure torque in the LDA point to the difficulty of determining the relevant topographic scales (for instance, *Bishop et al*. [2012] show how smaller-scale topography may influence the mesoscale flow) and estimating bottom pressure torque at a local level, even with near-bottom current measurements. The total Drake Passage bottom pressure torque is less sensitive to the scale of topography, as it is dominated by flow over the northern continental slope.

In the cDrake PFZ, both linear and nonlinear vorticity advection magnitudes decrease enough with depth that, despite the widespread turning with depth and offsets between surface and deep circulation patterns (section 4), the cDrake depth-integrated vorticity advection terms resemble the surface vorticity advection terms (not shown). Correlations between surface and depth-integrated advection terms in the PFZ are $r \geq 0.8$, and surface mean relative vorticity advection is approximately twice as large as surface eddy vorticity advection, and an order of magnitude larger than surface planetary vorticity advection. Thus, both the relative sizes and spatial patterns of the three vorticity advection terms (Figures 9a–9c) are represented in the surface fields (Figures 6b and 6c, βv not shown). However, we note that the sizes of the mean and eddy advection terms vary at different rates with depth, so that at longer scales (at least until the eddy advection term becomes unimportant, see section 7.3), the surface fields may not give an accurate picture of the depth-integrated totals.

The sensitivity of bottom pressure torque to the bottom current angle implies that its spatial and temporal patterns are likely to be misrepresented by extrapolation from surface velocity, even in regions of equivalent-barotropic flow where the current turns only slightly with depth. This sensitivity, along with the sensitivity to topography and the greater tendency for currents to turn with depth in observations (cDrake and those discussed by *Ferrari et al*. [2012] and *Phillips and Bindoff* [2014]) than in models [e.g., *Hughes and Killworth*, 1995; *Killworth and Hughes*, 2002; *Peña-Molino et al*., 2014], suggest care in interpreting bottom pressure torques from numerical models and state estimates with inadequate resolution [*Hughes*, 1995]. Bottom pressure torque in the LDA resembles surface or near-surface relative vorticity advection, both in

the time series (compare bottom pressure torque in Figure 8d with shallow advection in Figure 8a) and in the time mean (compare bottom pressure torque in Figure 9d with shallow advection terms in Figures 6b and 6c). Therefore, as suggested by *Hughes* [2005], in the absence of near-bottom data, bottom pressure torque may be better predicted as the residual of the surface relative and planetary vorticity advection terms.

7.3. Relevance to Longer Time Periods and Larger Areas

In contrast to the results of *Hughes and de Cuevas* [2001] and *Hughes* [2005], in which bottom pressure torque in Drake Passage is balanced principally by planetary vorticity advection, the cDrake bottom pressure torque is much larger than planetary vorticity advection, and instead is balanced by nonlinear relative vorticity advection. However, the cDrake array covers only a limited area; the portion of the LDA where we can calculate the higher-derivative terms of the vorticity balance is even smaller. The results described in sections 6 and 7.1 apply as well to the LDA as a whole as to the lowest-uncertainty region in the interior of the LDA, but even so are limited to approximately one meander wavelength (∼250 km) in the PFZ. In addition, although the circulation patterns observed over 4 years in cDrake were remarkably stable, if they were not persistent over longer time periods, the 4-year balance might not represent the spatial scales and relative sizes of mean and eddy terms of the long-term balance.

Based on the results described above (section 7.2) confirming that vorticity advection terms derived from surface fields are representative of the patterns and relative sizes of the depth-integrated advection terms, we use the 21-year satellite MADT to address the applicability of the cDrake results to greater temporal and spatial scales. The dominant feature of the cDrake mean circulation in the LDA, a southward meander of the SAF and northward meander of the PF, varies in strength over the MADT time series; *Ferrari et al*. [2012] found a similar pattern as the first EOF of the 18-year satellite sea level anomaly record in this area. The 21-year mean surface geostrophic stream function, however, although smoother than the 4-year average shown in Figure 5c, still exhibits the mean circulation patterns observed during the cDrake time period, in particular the distinct SAF and PF jets and the meanders in the LDA. Like the SOSE and cDrake geostrophic stream functions, it contains complex structure at a range of scales throughout Drake Passage and the Scotia Sea.

Surface vorticity gradient and vorticity advection terms (not shown) estimated by objective mapping or finite differencing of 1/4° MADT fields imply that mean and eddy relative vorticity advection dominate over planetary vorticity advection at a range of scales. When vorticity balance terms are computed from the 1/4° field before any additional smoothing (recalling that the 1/4° product incorporates mapping length scales of ∼100 km) [*Ducet et al*., 2000], mean relative vorticity advection dominates over planetary vorticity advection even when the terms are subsequently smoothed by Gaussian weighted averaging with length scales up to 300 km. Eddy relative vorticity advection is also first order at scales up to 150 km.

The first-order contribution of eddy relative vorticity advection to the cDrake balance (Figure 9), and its size in the MADT surface advection terms at longer scales, are consistent with the results of Williams et al. [2007] on the importance of eddy vorticity forcing in this region. The dominance of nonlinear relative vorticity advection over planetary vorticity advection to scales of a few hundred kilometers is also broadly consistent with the vorticity balance in an eddy-resolving model described by *Thompson and Naveira Garabato* [2014]. The MADT-derived mean relative vorticity advection, however, appears to contain more energy at larger spatial scales, and the clear scale separation between balances dominated by nonlinear versus linear vorticity advection terms reported by *Thompson and Naveira Garabato* [2014] is not evident.

7.4. Implications for the Overall ACC Vorticity Balance

The cDrake observations show a dominance of nonlinear over linear relative vorticity advection both in the time mean balance at scales of ∼50 km (Figure 9), and in the time-varying balance averaged over ∼250 km across the LDA, while the MADT-derived surface fields imply that this dominance persists both in the long-term time mean and to scales of ∼300 km. The discrepancy between these results and studies finding larger linear than nonlinear vorticity advection in Drake Passage [e.g., *Hughes and de Cuevas*, 2001; *Hughes*, 2005] is likely due to the effect of smaller-scale flows on the larger-scale balance by way of spatial correlations in the nonlinear terms [*Thompson and Naveira Garabato*, 2014]. While it is possible that this effect is more pronounced in Drake Passage and similar regions and less significant in the more open, meandering regions of

the ACC (for instance, *Grezio et al*. [2005] found nonlinear terms to be enhanced near topography), the results nevertheless emphasize the importance of nonlinear terms in the ACC vorticity balance.

The cDrake bottom pressure torque averages 3 to 4×10^{-9} m s^{-2}, more than an order of magnitude larger than the wind stress curl, providing observational confirmation for hypotheses and model results [e.g., *Wells and de Cuevas*, 1995; *Hughes and de Cuevas*, 2001; *Grezio et al*., 2005] suggesting that the whole ACC-integrated wind stress curl is balanced by bottom pressure torque from just two or three regions, including Drake Passage and the Scotia Sea. Interestingly, the cDrake observations imply that on average this bottom pressure torque is not generated over the Shackleton Fracture Zone, the large topographic ridge running across the passage, but almost entirely over the northern slope. *Masich et al*. [2015] reported that only 60% of the mean topographic form stress in SOSE is associated with submarine ridges, while 40% occurs across South America; the cDrake bottom pressure torque distribution implies that the continental slope is even more important as a vorticity sink than as a momentum sink in the ACC.

8. Summary and Conclusions

The cDrake CPIES dataset enables us to make maps of depth-varying and time-varying geostrophic stream function, velocity, relative vorticity, and relative vorticity gradients in Drake Passage, at horizontal scales down to 50 km. Fields in the PFZ just downstream of the SFZ are dominated by meander and eddy events, producing a 4-year mean circulation pattern of a cyclonic northward meander trough and anticyclonic southward meander crest, consistent with the first EOF of sea level anomaly as described by *Ferrari et al*. [2012] and exhibiting meander-related rotation of the currents with depth [as in *Lindstrom et al*., 1997; *Phillips and Rintoul*, 2000; *Tracey et al*., 2006; *Phillips and Bindoff*, 2014]. This mean circulation pattern is consistent enough that the time variability in vorticity is small relative to its spatial variability. The Rossby number of the time-varying geostrophic flow is large, up to 0.75 near the surface and 0.35 at the bottom. Although the Rossby number of the 4-year mean flow is $\mathcal{O}(0.1)$, the current departs significantly from equivalent-barotropic vertical structure over most of Drake Passage, even 200 km downstream of significant topography. Equivalent-barotropic mean flow is found mainly in the northern SAF, where both surface and near-bottom flow is nearly along-isobath along the steep continental slope.

The 4-year time series of near-bottom current measurements across Drake Passage, along with high-resolution multibeam bathymetry collected on the cDrake cruises, allowed us to estimate bottom pressure torque. Bottom pressure torque is strongly sensitive to the scale of topography used in the calculation; however, a range of estimates produce a time-mean, cross-passage-mean along the cDrake transect of 3 to 4×10^{-9} m s^{-2}, or 15–20 times the approximately 2×10^{-10} m s^{-2} mean wind stress curl forcing over the ACC. By far the largest contribution to bottom pressure torque over the cDrake array comes from strong near-bottom flow up the northern continental slope onto the South American shelf (Figure 4); the net contribution from the Shackleton Fracture Zone is small.

The vorticity balance in the high-*Ro* PFZ is dominated by relative vorticity advection and divergence at time scales of weeks to years. Depth integrals of both mean and eddy relative vorticity advection are $\mathcal{O}(10^{-7})$ m s^{-2}, while planetary vorticity advection is a tenth of that size. Bottom pressure torque in the PFZ is also $\mathcal{O}(10^{-7})$ m s^{-2} and is negatively correlated with nonlinear relative vorticity advection; however, it is only about one third of the total depth-integrated divergence, which arises mainly from the divergence of the ageostrophic component of gradient flow, contributed by the flow curvature. The cyclostrophic contribution to relative vorticity advection (the difference between geostrophic relative vorticity advection and relative vorticity advection based on the gradient wind velocity and vorticity fields) reduces the total relative vorticity advection by about 10%; the inclusion of curvature effects also produces qualitatively different horizontal divergence (otherwise absent for geostrophic flow) that is sufficiently large as to become the main balancing term for vorticity advection.

The transient eddy contribution to relative vorticity advection is significant at 50-km scale in the LDA; satellite altimeter data show it becomes second order at scales over about 200 km (section 7.3). In addition to the mesoscale geostrophic eddy contribution, even smaller-scale processes may need to be considered or at least parameterized in a full accounting of the ACC vorticity budget. The cyclostrophic contribution to gradient flow dynamics adds a second-order contribution to cDrake vorticity advection in the PFZ and a first-order contribution to the depth-integrated divergence; the observed bottom pressure torque is too

small to fully balance vorticity advection at 50-km scales in the PFZ. Bottom pressure torque is strongly sensitive to the scale of smoothing used for the topography as well as for the velocity field, but where it is strongest, on the northern slope, it is robust for a range of scales from 10 to 50 km. Principally due to flow on the northern slope, Drake Passage average bottom pressure torque exceeds wind stress curl by a factor of 15–20. The cDrake results provide observational confirmation of the importance of nonlinear terms and regions where the ACC interacts with major topographic features for the ACC vorticity balance.

Acknowledgments

The National Science Foundation Office of Polar Programs supported this work under NSF grants ANT-0636493/1141922 (SIO cDrake), ANT-0635437/1141802 (URI cDrake), ANT-0838750/1341431 (LMG ADCP program), and ANT-0961218 (SOSE). Y. Firing received support from the NASA Earth and Space Science Fellowship Program under grant NNX09AN87H. M. Mazloff acknowledges the NSF for support of this research through grants OCE-1234473 and PLR-1425989. SOSE was produced with support from NSF-XSEDE (Extreme Science and Engineering Discovery Environment) grant OCE130007. We thank K. Donohue and K. Tracey for their roles in the cDrake project, making the data used in this manuscript possible, and for many helpful discussions on the topics of this manuscript. We are grateful to G. Chaplin, S. Escher, D. Holloway, E. Sousa, E. Firing, J. Hummon, the captains and crew of the RVIB Nathaniel B. Palmer, the captains and crew of the ARSV Laurence M. Gould, and Raytheon Polar Services for technical and logistical support during the cruises. Data used in this work are listed in the text and references; cDrake data are available from the National Oceanographic Data Center (NODC, http://accession.nodc.noaa.gov/0121256) and the Marine Geoscience Data System (MGDS, http://www.marine-geo.org/index.php), SADCP data are available from the Joint Archive for Shipboard ADCP (JASADCP, ftp://ftp.soest.hawaii.edu/caldwell/adcp/INVNTORY/lmgould.html), SOSE outputs are available from http://sose.ucsd.edu/sose_stateestimation_data_05.html), and satellite data sources are given in the text.

References

Arbic, B. K., and R. B. Scott (2008), On quadratic bottom drag, geostrophic turbulence, and oceanic mesoscale eddies, *J. Phys. Oceanogr.*, *38*, 84–103, doi:10.1175/2007jpo3653.1.

Bishop, S. P., D. R. Watts, J.-H. Park, and N. G. Hogg (2012), Evidence of bottom-trapped currents in the Kuroshio Extension region, *J. Phys. Oceanogr.*, *42*, 321–328, doi:10.1175/JPO-D-11-0144.1.

Chereskin, T. K., K. A. Donohue, D. R. Watts, K. L. Tracey, Y. L. Firing, and A. L. Cutting (2009), Strong bottom currents and cyclogenesis in Drake Passage, *Geophys. Res. Lett.*, *36*, L23602, doi:10.1029/2009GL040940.

Chereskin, T. K., L. D. Talley, and B. M. Sloyan (2010), Nonlinear vorticity balance of the Subantarctic Front in the Southeast Pacific, *J. Geophys. Res.*, *115*, C06026, doi:10.1029/2009JC005611.

Chereskin, T. K., K. A. Donohue, and D. R. Watts (2012), cDrake: Dynamics and transport of the Antarctic Circumpolar Current in Drake Passage, *Oceanography*, *25*(3), 134–135.

Cunningham, S. A., S. G. Alderson, B. A. King, and M. A. Brandon (2003), Transport and variability of the Antarctic Circumpolar Current in Drake Passage, *J. Geophys. Res.*, *108*(C5), 8084, doi:10.1029/2001JC001147.

Ducet, N., P. Y. Le Traon, and G. Reverdin (2000), Global high-resolution mapping of ocean circulation from TOPEX/Poseidon and ERS-1 and -2, *J. Geophys. Res.*, *40*(C8), 19,477–19,498.

Ferrari, R., C. Provost, A. Renault, N. Sennéchael, N. Barré, Y.-H. Park, and J. H. Lee (2012), Circulation in Drake Passage revisited using new current time-series and satellite altimetry. Part I: The Yaghan basin, *J. Geophys. Res.*, *117*, C12024, doi:10.1029/2012JC008264.

Firing, Y. L., T. K. Chereskin, and M. R. Mazloff (2011), Vertical structure and transport of the Antarctic Circumpolar Current in Drake Passage from direct velocity observations, *J. Geophys. Res.*, *116*, C08015, doi:10.1029/2011JC006999.

Firing, Y. L., T. K. Chereskin, D. R. Watts, K. L. Tracey, and C. Provost (2014), Computation of geostrophic streamfunction, its derivatives, and error estimates from an array of CPIES in Drake Passage, *J. Atmos. Oceanic Technol.*, *31*, 656–680, doi:10.1175/JTECH-D-13-00142.1.

Foppert, A., K. A. Donohue, and D. R. Watts (2016), The Polar Front in Drake Passage: A composite-mean stream-coordinate view, *J. Geophys. Res.*, *121*, 1771–1788, doi:10.1002/2015JC011333.

Gill, A. E. (1968), A linear model of the Antarctic Circumpolar Current, *J. Fluid Mech.*, *32*, 465–488.

Grezio, A., N. C. Wells, V. O. Ivchenko, and B. A. de Cuevas (2005), Dynamical budgets of the Antarctic Circumpolar Current using ocean general-circulation models, *Q. J. R. Meteorol. Soc.*, *131*, 833–860, doi:10.1256/qj.03.213.

Holton, J. R. (1979), *An Introduction to Dynamic Meteorology*, Academic, Burlington, Mass.

Hughes, C. W. (1995), A warning about topography in the Cox code, *Ocean Modell.*, *106*, 8–11.

Hughes, C. W. (2005), Nonlinear vorticity balance of the Antarctic Circumpolar Current, *J. Geophys. Res.*, *110*, C11008, doi:10.1029/2004JC002753.

Hughes, C. W., and E. R. Ash (2001), Eddy forcing of the mean flow in the Southern Ocean, *J. Geophys. Res.*, *106*(C2), 2713–2722.

Hughes, C. W., and B. A. de Cuevas (2001), Why western boundary currents in realistic oceans are inviscid: A link between form stress and bottom pressure torques, *J. Phys. Oceanogr.*, *31*, 2871–2885.

Hughes, C. W., and P. D. Killworth (1995), Effects of bottom topography in the large-scale circulation of the Southern Ocean, *J. Phys. Oceanogr.*, *25*, 2485–2497.

Killworth, P. D. (1992), An equivalent-barotropic mode in the Fine Resolution Antarctic Model, *J. Phys. Oceanogr.*, *22*, 1379–1387.

Killworth, P. D., and C. W. Hughes (2002), The Antarctic Circumpolar Current as a free equivalent-barotropic jet, *J. Mar. Res.*, *60*, 19–45.

Lenn, Y.-D., T. K. Chereskin, J. Sprintall, and E. Firing (2007), Mean jets, mesoscale variability and eddy momentum fluxes in the surface layer of the Antarctic Circumpolar Current in Drake Passage, *J. Mar. Res.*, *65*, 27–58.

Lindstrom, S. S., X. Qian, and D. R. Watts (1997), Vertical motion in the Gulf Stream and its relation to meanders, *J. Geophys. Res.*, *102*(C4), 8485–8503, doi:10.1029/96JC03498.

Masich, J., T. K. Chereskin, and M. Mazloff (2015), Topographic form stress in the Southern Ocean State Estimate, *J. Geophys. Res.*, *120*, 7919–7933, doi:10.1002/2015JC011143.

Mazloff, M. R., P. Heimbach, and C. Wunsch (2010), An eddy-permitting Southern Ocean State Estimate, *J. Phys. Oceanogr.*, *40*, 880–899, doi:10.1175/2009JPO4236.1.

Meinen, C. S., and D. R. Watts (2000), Vertical structure and transport on a transect across the North Atlantic Current near 42°N: Time series and mean, *J. Geophys. Res.*, *105*(C9), 21,869–21,891.

Munk, W. H., and E. Palmén (1951), Note on the dynamics of the Antarctic Circumpolar Current, *Tellus*, *3*, 53–55.

Niiler, P. P., N. A. Maximenko, and J. C. McWilliams (2003), Dynamically balanced absolute sea level of the global ocean derived from near-surface velocity observations, *Geophys. Res. Lett.*, *30*(22), 2164, doi:10.1029/2003GL018628.

Nikurashin, M., and R. Ferrari (2010a), Radiation and dissipation of internal waves generated by geostrophic motions impinging on small-scale topography: theory, *J. Phys. Oceanogr.*, *40*, 1055–1074, doi:10.1175/2009JPO4199.1.

Nikurashin, M., and R. Ferrari (2010b), Radiation and dissipation of internal waves generated by geostrophic motions impinging on small-scale topography: Application to the Southern Ocean, *J. Phys. Oceanogr.*, *40*, 2025–2042, doi:10.1175/2010JPO4315.1.

Orsi, A. H., T. Whitworth III, and W. D. Nowlin Jr. (1995), On the meridional extent and fronts of the Antarctic Circumpolar Current, *Deep Sea Res., Part I*, *42*(5), 641–673.

Peña-Molino, B., S. R. Rintoul, and M. R. Mazloff (2014), Barotropic and baroclinic contributions to along-stream and across-stream transport in the Antarctic Circumpolar Current, *J. Geophys. Res.*, *119*, 8011–8028, doi:10.1002/2014JC010020.

Phillips, H. E., and N. L. Bindoff (2014), On the nonequivalent barotropic structure of the Antarctic Circumpolar Current: An observational perspective, *J. Geophys. Res.*, *119*, 5221–5243, doi:10.1002/2013JC009516.

Phillips, H. E., and S. R. Rintoul (2000), Eddy variability and energetics from direct current measurements in the Antarctic Circumpolar Current south of Australia, *J. Phys. Oceanogr.*, *30*, 3050–3076.

Ricciardulli, L., and F. Wentz (2011), Reprocessed QuikSCAT (V04) wind vectors with Ku-2011 geophysical model function, *Tech. Rep. 043011*, Remote Sens. Syst., Santa Rosa, Calif.

Rocha, C. B., T. K. Chereskin, S. T. Gille, and D. Menemenlis (2016), Mesoscale to submesoscale wavenumber spectra in Drake Passage, *J. Phys. Oceanogr.*, *46*, 601–620, doi:10.1175/JPO-D-15-0087.1.

Smith, W. H. F., and D. T. Sandwell (1997), Global seafloor topography from satellite altimetry and ship depth soundings, *Science*, *277*, 1957–1962.

Thompson, A. F., and A. C. Naveira Garabato (2014), Equilibration of the Antarctic Circumpolar Current by standing meanders, *J. Phys. Oceanogr.*, *44*, 1811–1828, doi:10.1175/JPO-D-13-0163.1.

Tracey, K. L., D. R. Watts, C. S. Meinen, and D. S. Luther (2006), Synoptic maps of temperature and velocity within the Subantarctic Front south of Australia, *J. Geophys. Res.*, *111*, C10016, doi:10.1029/2005JC002905.

Tracey, K. L., K. A. Donohue, D. R. Watts, and T. Chereskin (2013), cDrake CPIES data report, November 2007 to December 2011, *Tech. Rep. GSO 2013-01*, Grad. Sch. of Oceanogr., Univ. of R. I., Kingston.

Watts, D. R., K. L. Tracey, J. M. Bane, and T. J. Shay (1995), Gulf Stream path and thermocline structure near 74°W and 68°W, *J. Geophys. Res.*, *100*(C9), 18,291–18,312.

Watts, D. R., C. Sun, and S. Rintoul (2001), A two-dimensional gravest empirical mode determined from hydrographic observations in the Subantarctic Front, *J. Phys. Oceanogr.*, *31*, 2186–2209.

Wells, N. C., and B. A. de Cuevas (1995), Depth-integrated vorticity budget of the Southern Ocean from a general circulation model, *J. Phys. Oceanogr.*, *25*, 2569–2582.

Williams, R. G., C. Wilson, and C. W. Hughes (2007), Ocean and atmosphere storm tracks: The role of eddy vorticity forcing, *J. Phys. Oceanogr.*, *37*, 2267–2289, doi:10.1175/JPO3120.1.

Yelland, M., and P. K. Taylor (1996), Wind stress measurements from the open ocean, *J. Phys. Oceanogr.*, *26*, 541–558.

Yelland, M. J., B. I. Moat, P. K. Taylor, R. W. Pascal, J. Hutchings, and V. C. Cornell (1998), Wind stress measurements from the open ocean corrected for airflow distortion by the ship, *J. Phys. Oceanogr.*, *28*, 1511–1526.